

Supplementary Material

Large easy-axis magnetic anisotropy in a series of trigonal prismatic mononuclear cobalt (II) complexes with zero-field hidden single-molecule magnet behaviour: The important role of the distortion of the coordination sphere and intermolecular interactions on the slow relaxation

Aritz Landart-Gereka,^{a†} María Mar Quesada-Moreno,^{a†} Ismael F. Díaz Ortega,^{b,c} Hiroyuki Nojiri,^b Mykhaylo Ozerov,^d J. Krzystek,^{*d} María A. Palacios,^{*a} Enrique Colacio^{*a}

^a*Departamento de Química Inorgánica, Facultad de Ciencias, Universidad de Granada, 18071 Granada, Spain. E-mail: ecolacio@ugr.es, mpalacios@ugr.es*

^b*Institute for Materials Research, Tohoku University, Katahira, Sendai, 980-8577, Japan.*

^c*Departamento de Química y Física-CIESOL, Universidad de Almería, Ctra. Sacramento s/n, 04120, Almería.*

^d*National High Magnetic Field Laboratory, Florida State University, Tallahassee, Florida 32310, USA. Email: krzystek@magnet.fsu.edu*

† These authors contributed equally to this work.

Experimental

Synthetic procedures

General procedures: All reactions were conducted in oven-dried glassware in aerobic conditions and the analytical reagents were purchased from commercial sources and used without further purification. The precursor tris(methylhydrazido)phosphorylsulfide, (S)P[N(Me)NH₂]₃, was prepared according to a previously described procedure.²³ The ligand (S)P[N(Me)N=C(H)Py]₃ was prepared according to previously reported method,²³ modified as follows:

Synthesis of ligand (S)P[N(Me)N=C(H)Py]₃ (L)

Tris(methylhydrazido)phosphorylsulfide (0.5 g, 2.5 mmol), 2-pyridincarboxaldehyde (0.810 g, 7.5 mmol) and a few drops of acetic acid were refluxed in methanol (20 ml) for 4 hours, and, after cooling, were stirred overnight. Then, the mixture was evaporated to dryness and the resulting oil was extracted three times in dichloromethane with water. The filtrate was again evaporated to dryness and the purified oil was dissolved in the

minimum quantity of dichloromethane and precipitated with diethylether. The solid formed was filtered off, washed with diethylether and dried in vacuum. Yield: 38%. Anal. Calc. for $C_{21}H_{24}N_9PS$: C, 54.18; H, 5.20; N, 27.08; S, 6.89. Found: C, 53.87; H, 4.95; N, 26.88; S, 6.65. IR (cm^{-1}): 3000-2800, $\nu(CH)$; 1600-1400, $\nu(C=C$ and $C=N)$ and 950 $\nu(P=S)$. 1H NMR ($CDCl_3$, ppm): 8.5 (d, H_{py}), 7.8 (s, H_{imine}), 7.6 (d, H_{py}), 7.3 (m, H_{py}), 7.1 (m, H_{py}), 3.4 (s, H_{methyl}).

Synthesis of $[Co(L)][CoCl_4] \cdot CH_3CN$ (1)

A solution of $CoCl_2 \cdot 6H_2O$ (15 mg, 0.065 mmol) in 10 ml of acetonitrile was added in continuous stirring to a solution of the ligand (30 mg, 0.065 mmol) in acetonitrile (10 ml). X-Ray quality green crystals of 1 were obtained after slow evaporation of the solution at room temperature. Yield: 31%. Anal. Calc. for $C_{23}H_{27}Cl_4Co_2N_{10}PS$: C, 36.05; H, 3.55; N, 18.28; S, 4.18. Found: C, 36.01; H, 3.38; N, 18.51; S, 4.04. IR (cm^{-1}): 3000-2800, $\nu(CH)$; 1600-1400, $\nu(C=C$ and $C=N)$ and 950, $\nu(P=S)$.

Synthesis of $[Co(L)][ZnCl_4] \cdot CH_3OH$ (2)

To a solution of the ligand (30 mg, 0.065 mmol) in 10 mL of MeOH were subsequently added with continuous stirring 15 mg (0.065 mmol) of $CoCl_2 \cdot 6H_2O$ in methanol (5 ml) and 9 mg (0.065 mmol) of $ZnCl_2$ in 5 ml of methanol. After few days, well-formed orange crystals of 2 were obtained by diffusion of hexane into the mother liquid. Yield: 37%. Anal. Calc. for $C_{22}H_{28}Cl_4CoN_9OPSZn$: C, 34.60; H, 3.70; N, 16.51; S, 4.20. Found: C, 34.57; H, 3.72; N, 16.56; S, 4.10. IR (cm^{-1}): 3000-2800, $\nu(CH)$; 1600-1400, $\nu(C=C$ and $C=N)$ and 950, $\nu(P=S)$.

Synthesis of $[Co(L)](ClO_4)_2 \cdot 2CH_3OH$ (3)

This compound was prepared following the same method as for compound 1 but using $Co(ClO_4)_2 \cdot 6H_2O$ (24 mg, 0.065 mmol) and methanol instead of $CoCl_2$ and acetonitrile. After few days, suitable orange crystals for X-ray diffraction were obtained. Yield: 31%. Anal. Calc. for $C_{23}H_{32}Cl_2CoN_9O_{10}PS$: C, 35.08; H, 4.10; N, 16.01; S, 4.07. Found: C, 35.05; H, 4.32; N, 15.93; S, 4.00. IR (cm^{-1}): 3000-2800, $\nu(CH)$; 1600-1400, $\nu(C=C$ and $C=N)$; 1100, $\nu(Cl-O)$ and 950, $\nu(P=S)$.

Synthesis of $[Co(L)](BF_4)_2$ (4)

This complex was obtained following the same procedure as for 3 but using $Co(BF_4)_2 \cdot 6H_2O$ (22 mg, 0.065 mmol) instead of $Co(ClO_4)_2 \cdot 6H_2O$. After 72 h, orange crystals suitable for X-ray diffraction were obtained by diffusion of isopropanol into the mother solution. Yield: 49%. Anal. Calc. for $C_{21}H_{24}B_2CoF_8N_9PS$: C, 36.13; H, 3.47; N, 18.06; S, 4.59. Found: C, 36.10; H, 3.44; N, 18.04; S, 4.77. IR (cm^{-1}): 3000-2800, $\nu(CH)$; 1600-1400, $\nu(C=C$ and $C=N)$; 1100 and 1000, $\nu(B-F)$ and 950, $\nu(P=S)$.

Synthesis of $[Co(L)(SCN)_2]$ (5)

To a solution of the ligand (30 mg, 0.065 mmol) in 10 ml of MeOH was added with continuous stirring $\text{Co}(\text{SCN})_2$ (11 mg, 0.065 mmol) in MeOH (10 ml) and an orange precipitate immediately appeared. The solid was dissolved adding CH_3CN to the mixture. After filtering to eliminate any amount of solid material, the solution was kept at room temperature. X-ray quality orange crystals of **5** were obtained by slow evaporation of the solution after several days. Yield: 43%. Anal. Calc. for $\text{C}_{23}\text{H}_{24}\text{CoN}_{11}\text{PS}_3$: C, 43.12; H, 3.78; N, 24.05; S, 15.02. Found: C, 42.84; H, 4.20; N, 24.11; S, 15.32. IR (cm^{-1}): 3000-2800, $\nu(\text{CH})$; 2100, $\nu(\text{SCN})$; 1600-1400, $\nu(\text{C}=\text{C}$ and $\text{C}=\text{N})$ and 950, $\nu(\text{P}=\text{S})$.

Synthesis of the diluted samples **3'** and **4'**

These compounds were prepared following the same method as for compound **3** but using a 1:6 Co/Zn ratio that is, 2.4 mg of $\text{Co}(\text{ClO}_4)_2 \cdot 6\text{H}_2\text{O}$ (0.0065 mmol) and 12.10 mg of $\text{Zn}(\text{ClO}_4)_2 \cdot 6\text{H}_2\text{O}$ (0.0325 mmol) for **3'** and 2.2 mg of $\text{Co}(\text{BF}_4)_2 \cdot 6\text{H}_2\text{O}$ (0.0065 mmol) and 7.7 mg of $\text{Zn}(\text{BF}_4)_2 \cdot \text{H}_2\text{O}$ (0.0325 mmol) for **4'**. In both cases, a pale orange solid immediately precipitated. The XRPD spectra demonstrate that the compounds are isostructural with respect to the undiluted complexes (see Fig. S1). The experimental Co/Zn ratios for these compounds extracted from dc magnetic data were found to be 1/6.2 and 1/6.3 for **3'** and **4'**, respectively (Figure S1).

Physical measurements

Elemental analyses were performed on a Fisons-Carlo Erba analyser model EA 1108 and ^1H -NMR spectra on a 400 Hz "VARIAN DIRECT DRIVE" spectrometer at the "Centro de Instrumentación Científica" (University of Granada). IR spectra were recorded on a Bruker Tensor 27 spectrophotometer by using ATR detection. The X-ray powder diffraction (XRPD) spectra were registered on a (2 θ) Bruker D2-PHASE using $\text{CuK}\alpha$ ($\lambda = 1.5418 \text{ \AA}$) radiation and LINXEYE detector, from 5 to 50° (2 θ) at a scanning rate of 0.5 ° 2 θ /min.

The *dc* magnetic measurements were performed on polycrystalline samples of **1-5**, **3'** and **4'** in the temperature range 2 - 300 K under a magnetic field of 0.1 T (20 - 300K) and 0.05 T (40 - 2K) using a Quantum Design SQUID MPMS XL-5. Alternating-current (ac) susceptibility measurements under different applied static fields (0-0.3 T) were carried out using a Quantum Design SQUID MPMS XL-5 magnetometer and a PPMS-9 susceptometer on polycrystalline samples in the temperature range 2-25 K. For compounds **1-5**, measurements were performed under an oscillating field of 3.5 Oe and *ac* frequencies in the 10 -1500 Hz (SQUID MPMS XL-5), whereas *ac* measurements on **3'** and **4'** were recorded within the frequency range 50 - 10000 Hz under an oscillating

field of 5 Oe (PPMS-9). The magnetic susceptibility values were corrected for the diamagnetism of the molecular constituents and sample holder.

Far-infrared magnetic spectroscopy (FIRMS, also known as frequency-domain THz EPR spectroscopy²⁴) experiments were performed at the National High Magnetic Field Laboratory using a Bruker Vertex 80v FT-IR spectrometer coupled with a 17 T vertical-bore superconducting magnet in a Voigt configuration (light propagation perpendicular to the external magnetic field). The experimental setup employs broad band terahertz radiation emitted by a mercury arc lamp. The radiation transmitted through the sample was detected by a composite silicon bolometer (Infrared Laboratories) mounted at the end of the quasioptical transmission line. Both sample and bolometer were cooled by a low-pressure helium gas to the temperature of 5 K. The intensity spectra of the microcrystalline powder sample (~2 mg) bonded by n-eicosane were measured in the spectral region between 14 and 730 cm⁻¹ (0.42–22 THz) with an instrumental resolution of 0.3 cm⁻¹ (9 GHz). To discern the magnetic absorptions, the transmission spectrum at each magnetic field was divided by the reference spectrum, which is calculated as the average spectrum for all magnetic fields after removing outlier points at each frequency. Such normalized spectra are only sensitive to tiny transmission changes induced by the magnetic field and exclude a strong nonmagnetic contribution due to vibrational absorptions and an instrumental function. All data analysis routine was implemented by in-house written MATLAB code based on the EPR simulation software package EasySpin.²⁵

High-frequency and -field EPR (HFEPR) spectra of compounds **1-5** were recorded at the National High Magnetic Field Laboratory in a 4.5-10 K temperature range on polycrystalline samples (20–25 mg), using a homodyne spectrometer at the EMR facility associated with a 15/17-T superconducting magnet and a frequency range from 52 to 426 GHz. Detection was provided with an InSb hot electron bolometer (QMC Ltd., Cardiff, UK). The magnetic field was modulated at 50 kHz for detection purposes. A Stanford Research Systems SR830 lock-in amplifier converted the modulated signal to *dc* voltage. The single-frequency spectra as well as their dependencies on frequency were simulated with the SPIN software from A. Ozarowski.

Single-Crystal Structure Determinations

Suitable crystals of **1-5** were mounted on a glass fiber and used for data collection. X-ray diffraction data were collected at 100 K using a Bruker D8 Venture diffractometer (MoK α radiation, $\lambda = 0.71073 \text{ \AA}$) outfitted with a PHOTON 100 detector. Unit-cell parameters were determined and refined on all observed reflections using APEX2

software.²⁶ Correction for Lorentz polarization and absorption were applied by SAINT²⁷ and SADABS²⁸ programs, respectively.

The structures were solved by direct methods and refined by the full-matrix least-squares method on F² using OLEX2 program.²⁹ All non-hydrogen atoms were refined anisotropically. Hydrogen atom positions were calculated and isotropically refined as riding models to their parent atoms. The ClO₄⁻ and BF₄⁻ counteranions in structures **3** and **4** are disordered (O1, O6, O8 atoms for **3** and F5, F6, F7, F8 atoms for **4**) and the disorder model was not satisfactory. Moreover, in the methanol molecule belonging to structure **2** and in one of the methanol molecules in structure **3**, the peak corresponding to the oxygen atom was not clear even with free occupancy and could not be modelled using discrete atoms, so that the disorder model was not obvious. This causes checkCIF alerts concerning chemical formula. A summary of selected data collection and refinement parameters can be found from the Supporting Information (Table S10) and CCDC 2144913-2144917.

Computational methodology

Calculations were carried out from the crystallographic structures using the cif files. The electronic structure and magnetic properties have been computed using state averaged complete active space self-consistent field calculations (SA-CASSCF (7,5)),³⁰ followed by the N-electron valence second-order perturbation theory (NEVPT2) method³¹ with the def2-TZVPP basis set,³² including the auxiliary basis sets for correlation and Coulomb fitting for all the atoms. All calculations were done with the ORCA 4.0.1.2 quantum chemistry program package.³³ Spin Hamiltonian parameters (*D*, *E* and *g*-tensor) were computed using the effective Hamiltonian $S=3/2$. In this case, spin-orbit effects were included using the quasi-degenerate perturbation theory (QDPT)^{34,35} and scalar relativistic effects were taken into account using the DKH (Douglas-Kroll-Hess) procedure.³⁶ The employed active space includes seven electrons in five 3d-orbitals of Co(II) CAS (7,5). We have included all 10 states for the $2S+1=4$ (quartet) states arising from the ⁴F and ⁴P terms of Co(II), and all the 40 states for the respective $2S+1=2$ (duplet) states arising from the ²P, ²D (twice), ²F, ²G and ²H terms of the Co(II) ion. ORCA produces two sets of results CASSCF and NEVPT2. The splitting of d-orbitals due to ligand field has been computed with the *ab initio* ligand field theory (AILFT)³⁷ module implemented in ORCA program package.

Pulse-field magnetization

Low-temperature magnetization measurements were performed by means of a conventional inductive probe in pulsed-magnetic fields. The temperature was reached as low as 0.4 K using a ^3He cryostat.³⁸ Polycrystalline specimens were mounted in a capillary tube made of polyimide. Samples of approximately 20 mg were not fixed within the sample tube and then they aligned along the magnetic field direction. Subsequently, a magnetic field was applied several times until orientation effect was saturated and the magnetization curves obtained in further shots were found to be identical.

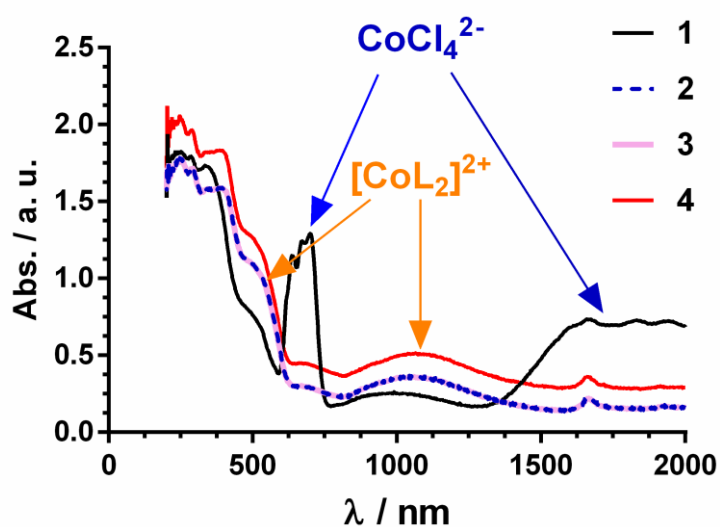


Figure S1.- Reflectance diffuse spectra of complexes 1-4, with indication of the origin of the observed bands

Table S1: Selected bond distances and angles for **1-4**

| Selected bond distances (Å) | | | | |
|-----------------------------|------------|-----------|------------|------------|
| | 1 | 2 | 3 | 4 |
| Co-N4 | 2.1151(17) | 2.140(2) | 2.1343(18) | 2.155(4) |
| Co-N5 | 2.1246(17) | 2.155(2) | 2.1575(19) | 2.169(4) |
| Co-N6 | 2.1442(17) | 2.157(2) | 2.1575(16) | 2.122(6) |
| Co-N7 | 2.1249(18) | 2.159(2) | 2.1600(17) | 2.147(5) |
| Co-N8 | 2.1349(17) | 2.130(2) | 2.1442(17) | 2.130(6) |
| Co-N9 | 2.0861(17) | 2.156(2) | 2.1216(18) | 2.158(5) |
| Selected bond angles (°) | | | | |
| | 1 | 2 | 3 | 4 |
| N4-Co-N5 | 83.59(7) | 83.07(8) | 81.48(7) | 83.27(17) |
| N4-Co-N6 | 86.32(7) | 83.64(9) | 83.09(7) | 83.3(2) |
| N4-Co-N7 | 76.42(7) | 75.46(8) | 75.89(7) | 75.9(2) |
| N4-Co-N8 | 150.90(7) | 149.21(9) | 145.59(7) | 117.4(2) |
| N4-Co-N9 | 116.38(7) | 114.52(8) | 118.09(7) | 148.67(19) |
| N5-Co-N6 | 83.10(6) | 83.02(8) | 85.06(7) | 83.05(18) |
| N5-Co-N7 | 111.81(7) | 115.92(8) | 110.81(7) | 149.5(2) |
| N5-Co-N8 | 76.27(6) | 76.12(8) | 75.76(7) | 76.31(18) |
| N5-Co-N9 | 150.06(7) | 150.38(8) | 149.82(7) | 117.07(18) |
| N6-Co-N7 | 155.33(7) | 149.19(8) | 151.02(7) | 115.8(2) |
| N6-Co-N8 | 111.44(7) | 115.47(8) | 119.64(7) | 148.18(18) |
| N6-Co-N9 | 76.64(7) | 75.97(8) | 75.61(7) | 76.4(2) |
| N7-Co-N8 | 91.68(6) | 93.43(8) | 88.40(7) | 93.6(2) |
| N7-Co-N9 | 95.20(7) | 92.26(8) | 96.84(7) | 91.6(2) |
| N8-Co-N9 | 90.79(7) | 94.21(8) | 93.76(7) | 91.6(2) |

Table S2: Selected bond distances and angles for complex **5**

| Selected bond distances (Å) | | | |
|-----------------------------|------------|-----------|------------|
| Co-N4 | 2.1887(15) | Co-N5 | 2.1604(15) |
| Co-N7 | 2.1511(15) | Co-N8 | 2.1587(16) |
| Co-N10 | 2.0519(16) | Co-N11 | 2.1001(15) |
| Selected bond angles (°) | | | |
| N4-Co-N5 | 92.42(6) | N4-Co-N7 | 77.15(6) |
| N4-Co-N8 | 167.28(6) | N4-Co-N10 | 100.67(6) |
| N4-Co-N11 | 87.36(6) | N5-Co-N7 | 168.27(6) |
| N5-Co-N8 | 76.76(6) | N5-Co-N10 | 99.87(6) |
| N5-Co-N11 | 84.49(6) | N7-Co-N8 | 112.87(6) |
| N7-Co-N10 | 87.49(6) | N7-Co-N11 | 89.61(6) |
| N8-Co-N10 | 87.93(6) | N8-Co-N11 | 84.98(6) |
| N10-Co-N11 | 170.63(6) | | |

Table S3: Shape measures for CoN₆ coordination sphere in complexes **1-5**

| Complex | JPPY-6 | TPR-6 | OC-6 | PPY-6 | HP-6 |
|---------|--------|--------|-------|--------|--------|
| 1 | 22.470 | 3.839 | 5.833 | 18.834 | 35.508 |
| 2 | 22.377 | 3.196 | 6.858 | 18.342 | 36.334 |
| 3 | 21.110 | 3.002 | 7.304 | 17.501 | 34.615 |
| 4 | 21.786 | 2.759 | 7.368 | 18.165 | 36.175 |
| 5 | 24.352 | 12.028 | 1.803 | 21.549 | 26.396 |

JPPY-6: Johnson Pentagonal Pyramid J2 (C_{5v}); TPR-6: Trigonal Prism (D_{3h});

OC-6: Octahedron (O_h); PPY-6: Pentagonal Pyramid (C_{5v}); HP-6: Hexagon (D_{6h})

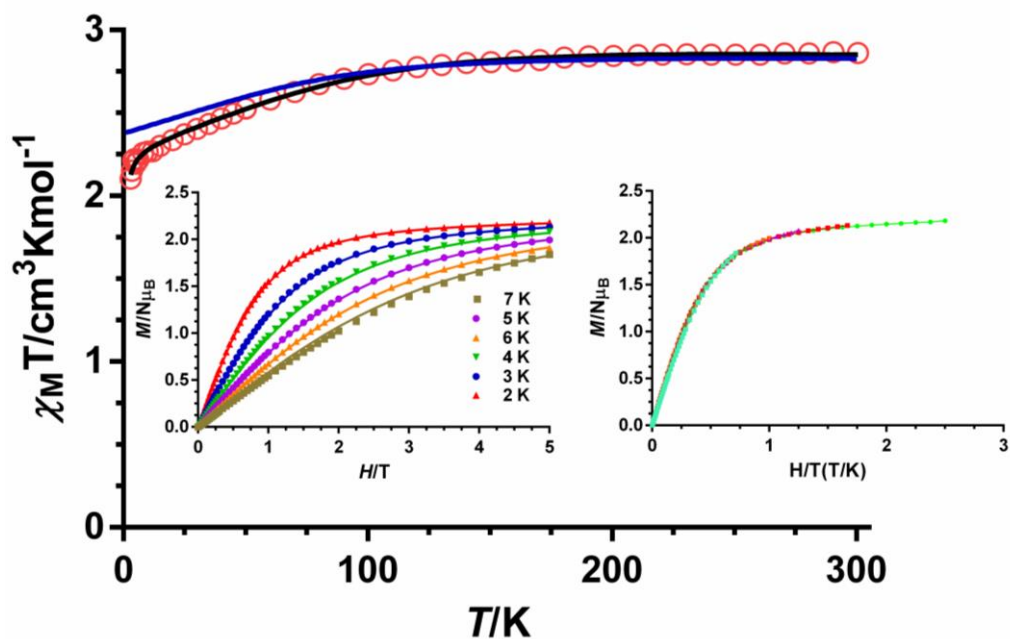


Figure S2.-Temperature dependence of $\chi_M T$ for compound **3** (red circles). Field dependence of magnetization at the indicated temperatures (inset left) and M vs H/T isotherms (inset right). Solid lines represent the best fit to equation 1 with the parameters indicated in Table 1. The blue solid line in the $\chi_M T$ vs T plot represents the *ab initio* calculated curve.

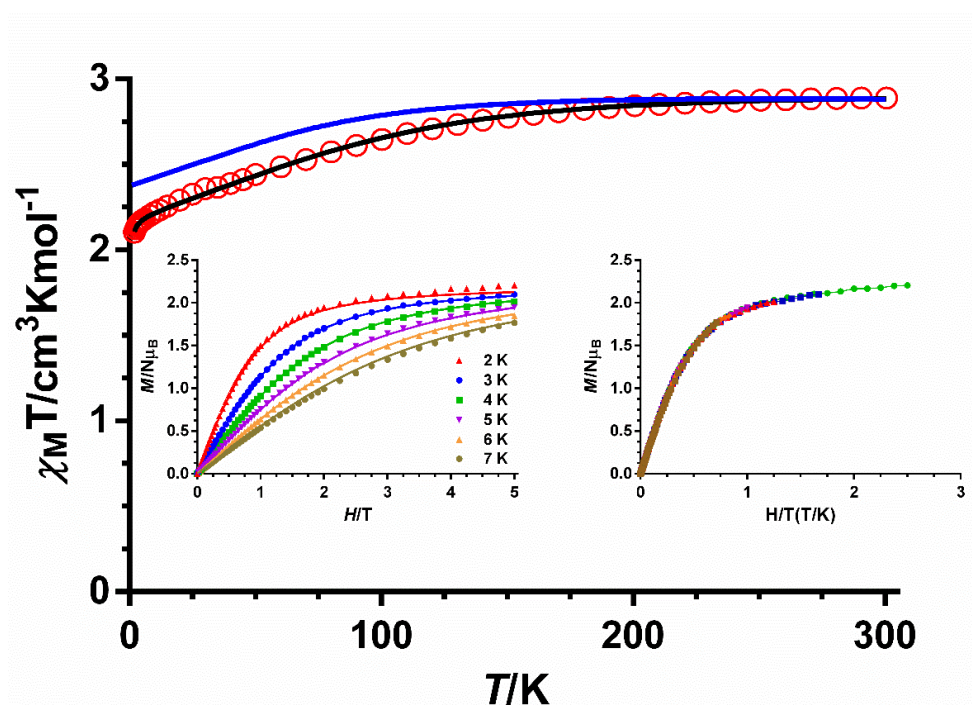


Figure S3.-Temperature dependence of $\chi_M T$ for compound **4** (red circles). Field dependence of magnetization at the indicated temperatures (inset left) and M vs H/T isotherms (inset right). Solid lines represent the best fit to equation 1 with the parameters indicated in Table 1. The blue solid line in the $\chi_M T$ vs T plot represents the *ab initio* calculated curve scaled by a factor of 0.9.

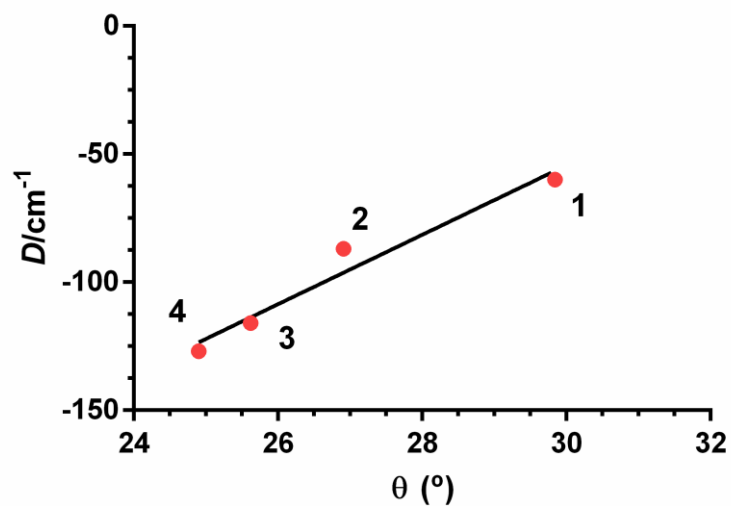


Figure S4.- Plot of the axial anisotropy parameter versus the Bailar angle (θ) for compounds 1-4. The black solid line represents the best linear fitting leading to the equation $D = 13.54 * (\theta) - 460.7$.

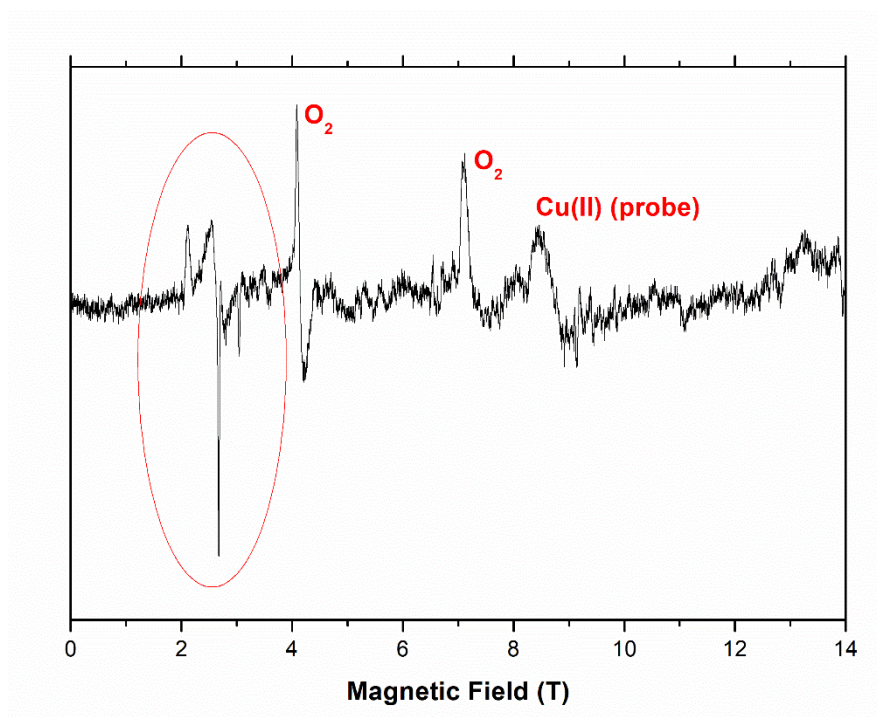


Figure S5.- HFEPR spectrum of 2 at 5 K and 261 GHz. The red oval marks Co(II) resonances.

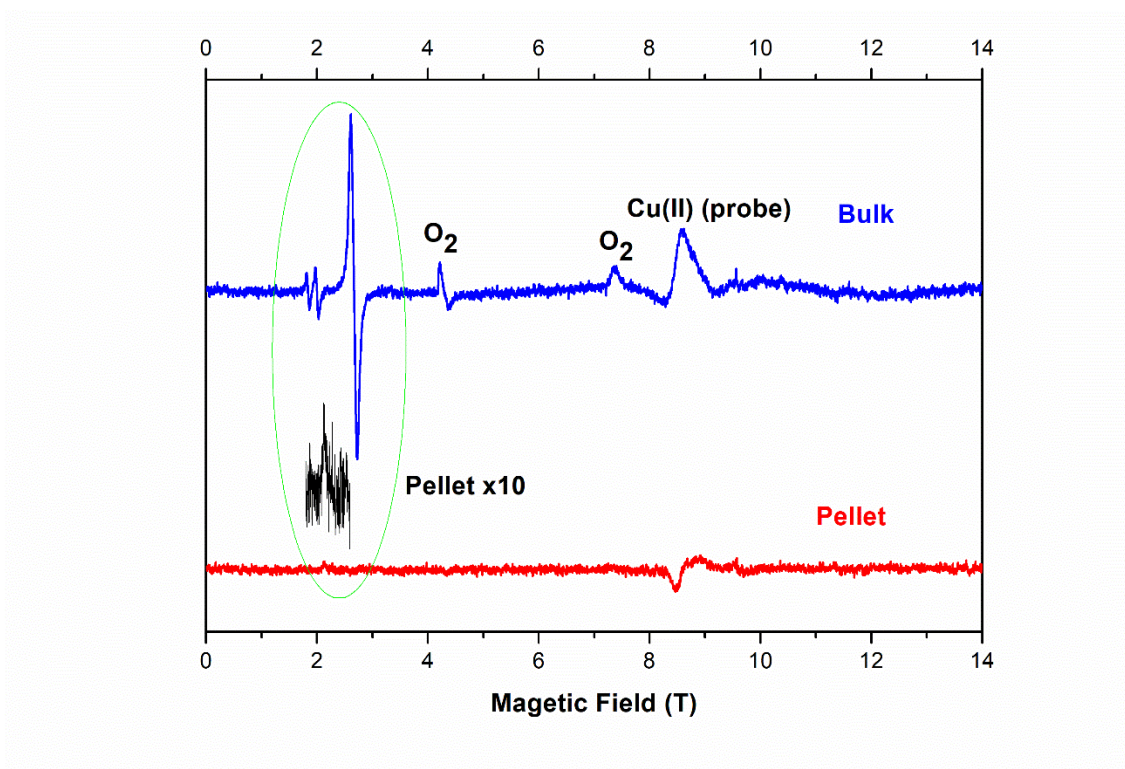


Figure S6.- HFEPR spectrum of **4** at 5 K and 261 GHz. The green oval marks Co(II) resonances.

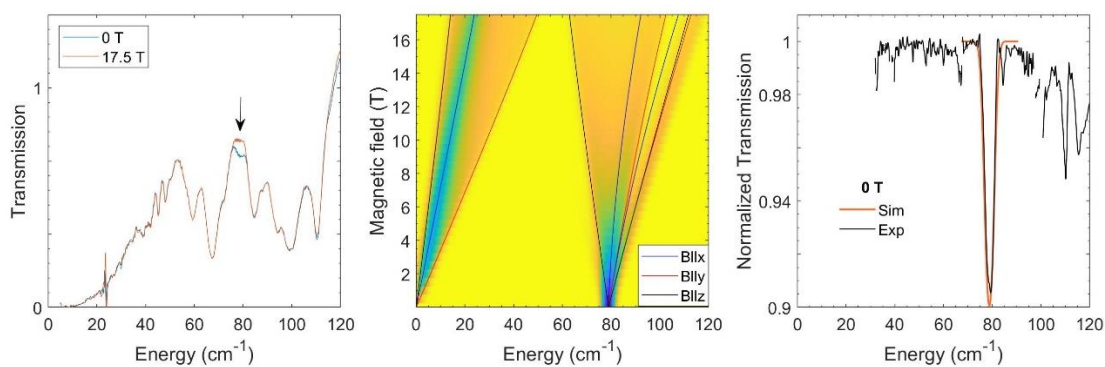


Figure S7.- FIRMS data for the compound **5**. Left panel shows far-infrared transmission spectra measured at two magnetic fields. The arrow indicates the position assigned to the zero-field energy. Middle panel shows the simulation of the 2D magnetic resonance spectrum using spin Hamiltonian parameters same as for HFEPR data. The lines show the field dependence of the turning points. Right panel shows zero-field slices taken from simulated (middle) and experimental (Fig. 9 in the main text) 2D color map.

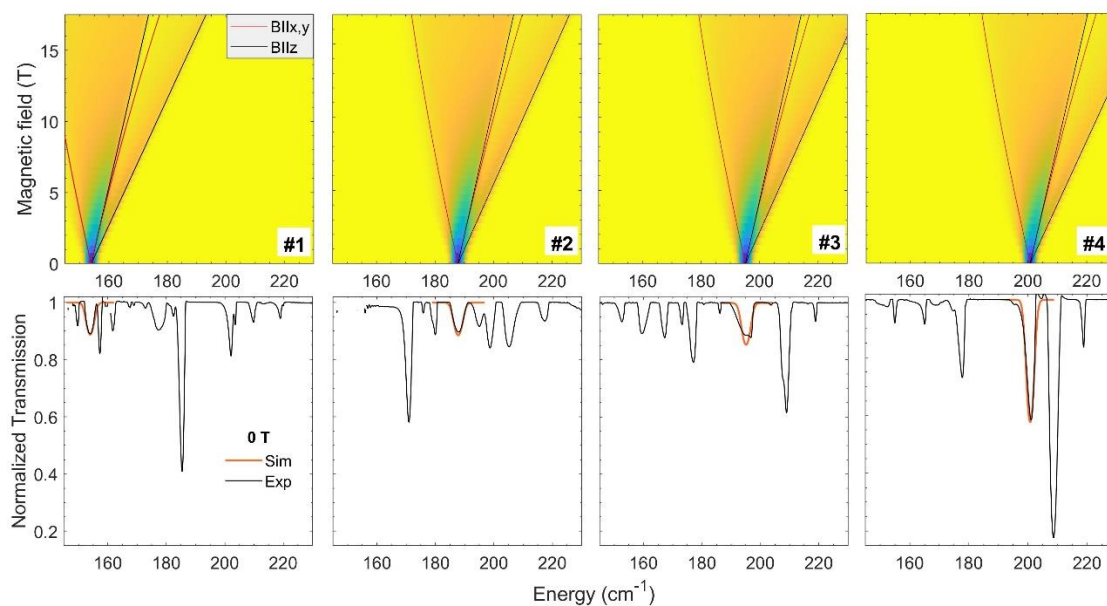


Figure S8.- Top panel shows the simulation of the powder spectrum of the magnetic resonance absorption. The $S=3/2$ spin-Hamiltonian model was using parameters $g_{iso}=2.4$, $E=0$, whereas the single ion anisotropy D parameter was taken as -76.9 , -93.9 , -97.4 -100.4 cm^{-1} from left to right. Red and black lines show field dependence of the magnetic resonance energy for the magnetic field applied along x and z axes of the D anisotropy tensor. Bottom panel shows a zero-field slice taken from the top panel superimposed with the experimental data taken from Fig. 10 in the main text. The zero-field energy is assigned to the peaks with similar amplitude and broadening for the compounds 1,2,3, taking into account the comparison of the simulated and experimental FIRMS patterns.

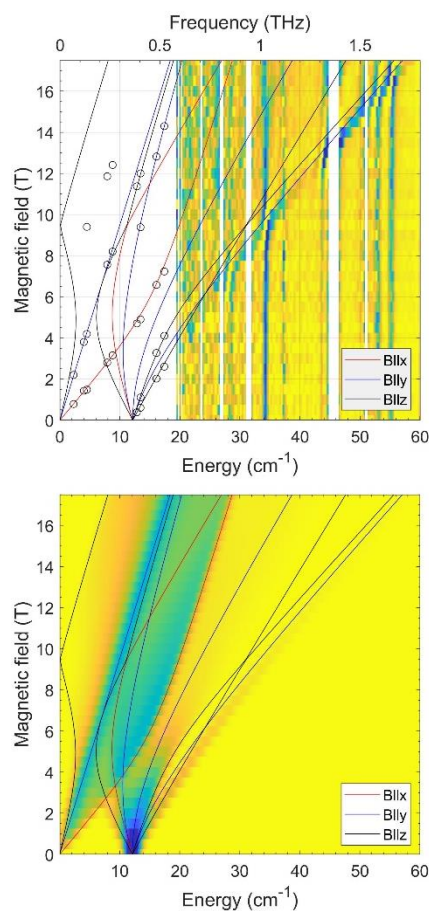


Figure S9.- (Top) Experimental part of the FIRMS spectrum of **1** corresponding to the CoCl_4^{2-} anion. (Bottom) Simulated spectrum with the D , E and g_i values extracted from the HFEPR spectra.

Table S4: Spin Free CASSCF energies (δE , cm^{-1})

| States | 1 | 2 | 3 | 4 | 5 |
|--------|----------|----------|----------|----------|----------|
| 1 | 560.6 | 599.2 | 450.6 | 426.8 | 1346.9 |
| 2 | 4407.1 | 4823.3 | 5118.5 | 5086.1 | 2148.1 |
| 3 | 10210.1 | 9223.4 | 8942.4 | 9302.7 | 10182.6 |
| 4 | 10464.8 | 9685.2 | 9931.8 | 9443.8 | 10477.1 |
| 5 | 11328.7 | 10445.7 | 10222.6 | 10214.1 | 10598.6 |

Table S5: Energy levels after the inclusion of spin-orbit effects (ΔE , cm^{-1})

| States | 1 | 2 | 3 | 4 | 5 |
|--------|----------|----------|----------|----------|----------|
| 1 | 184.27 | 183.07 | 215.73 | 219.32 | 98.10 |
| 2 | 814.38 | 853.85 | 760.60 | 746.21 | 1434.66 |
| 3 | 1060.04 | 1100.09 | 1037.70 | 1027.19 | 1569.98 |
| 4 | 4600.19 | 5001.41 | 5328.01 | 5304.44 | 2348.49 |
| 5 | 4682.81 | 5087.27 | 5417.98 | 5391.74 | 2394.41 |

Table S6: The ligand field one electron eigenfunctions for compounds **1-4** from NEVPT2 calculations and from CASSCF and NEVPT2 for **5**.

1

| Orbital | Energy (eV) | Energy (cm ⁻¹) | d_{xy} | d_{yz} | d_{z^2} | d_{xz} | $d_{x^2-y^2}$ |
|---------|-------------|----------------------------|-----------|-----------|-----------|-----------|---------------|
| 1 | 0.000 | 0.0 | -0.009307 | 0.000433 | -0.999904 | 0.006651 | 0.007813 |
| 2 | 0.118 | 949.1 | -0.881725 | -0.411458 | 0.010377 | 0.170153 | 0.155578 |
| 3 | 0.194 | 1565.9 | 0.177528 | -0.172718 | 0.003190 | -0.330590 | 0.910688 |
| 4 | 1.149 | 9263.6 | 0.436704 | -0.776586 | -0.001959 | 0.448742 | -0.069510 |
| 5 | 1.177 | 9493.5 | -0.015766 | -0.444731 | -0.008391 | -0.812616 | -0.376232 |

2

| Orbital | Energy (eV) | Energy (cm ⁻¹) | d_{xy} | d_{yz} | d_{z^2} | d_{xz} | $d_{x^2-y^2}$ |
|---------|-------------|----------------------------|-----------|-----------|-----------|-----------|---------------|
| 1 | 0.000 | 0.0 | -0.029930 | -0.004285 | 0.998505 | 0.032103 | -0.032303 |
| 2 | 0.133 | 1071.6 | 0.380705 | -0.155503 | 0.049238 | -0.353190 | 0.838877 |
| 3 | 0.188 | 1517.3 | 0.848170 | 0.343780 | 0.018976 | -0.135145 | -0.379208 |
| 4 | 1.020 | 8227.0 | -0.173754 | -0.295424 | 0.010478 | -0.873935 | -0.344474 |
| 5 | 1.074 | 8658.9 | 0.323397 | -0.877690 | -0.009692 | 0.303645 | -0.181053 |

3

| Orbital | Energy (eV) | Energy (cm ⁻¹) | d_{xy} | d_{yz} | d_{z^2} | d_{xz} | $d_{x^2-y^2}$ |
|---------|-------------|----------------------------|-----------|-----------|-----------|-----------|---------------|
| 1 | 0.000 | 0.0 | -0.038386 | -0.034115 | 0.998402 | 0.019351 | 0.013497 |
| 2 | 0.140 | 1128.7 | 0.880098 | 0.206656 | 0.050892 | -0.326053 | -0.271697 |
| 3 | 0.207 | 1667.9 | 0.289677 | -0.302728 | -0.008263 | -0.156513 | 0.894359 |
| 4 | 1.004 | 8099.9 | 0.328367 | -0.652739 | -0.019344 | 0.648000 | -0.214077 |
| 5 | 1.045 | 8430.0 | -0.179487 | -0.662131 | -0.012709 | -0.670011 | -0.283357 |

4

| Orbital | Energy (eV) | Energy (cm ⁻¹) | d_{xy} | d_{yz} | d_{z^2} | d_{xz} | $d_{x^2-y^2}$ |
|---------|-------------|----------------------------|-----------|-----------|-----------|-----------|---------------|
| 1 | 0.000 | 0.0 | 0.049167 | -0.004990 | 0.998036 | 0.010040 | 0.037171 |
| 2 | 0.138 | 1114.8 | -0.778021 | 0.360362 | 0.020432 | 0.074568 | 0.508767 |
| 3 | 0.191 | 1538.8 | 0.523742 | -0.035606 | -0.058391 | 0.338030 | 0.778943 |
| 4 | 1.006 | 8110.7 | -0.326458 | -0.725369 | 0.009160 | 0.601424 | -0.073962 |
| 5 | 1.061 | 8559.4 | -0.106699 | -0.585394 | -0.003729 | -0.719975 | 0.357144 |

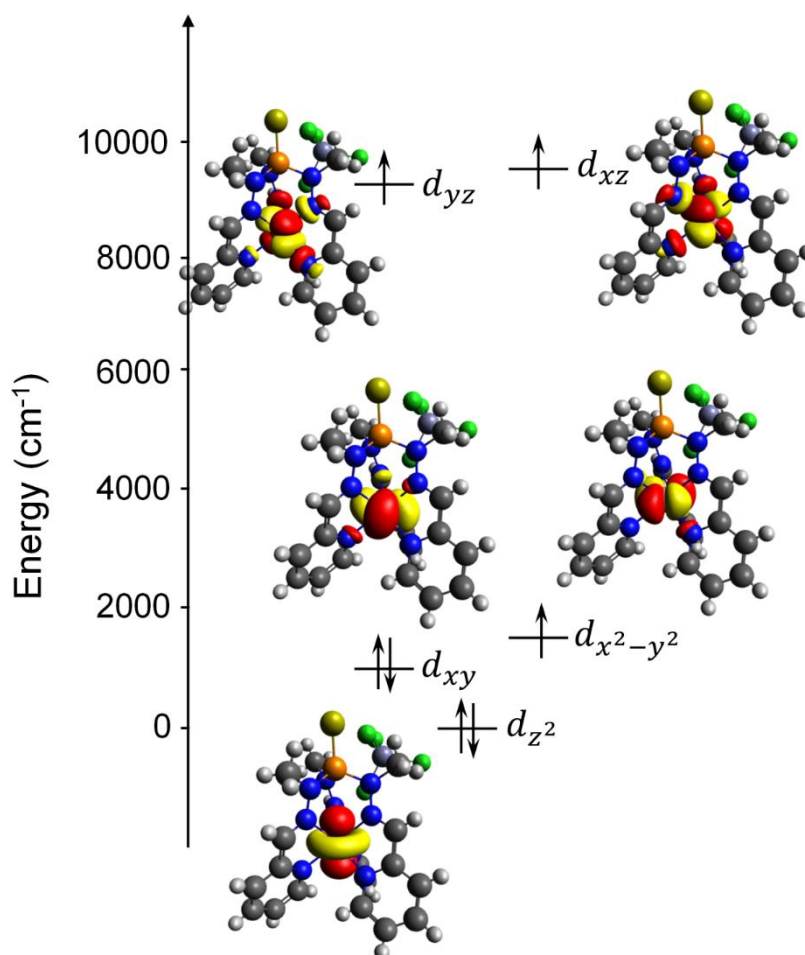
5 – CASSCF

| Orbital | Energy (eV) | Energy (cm ⁻¹) | d_{xy} | d_{yz} | d_{z^2} | d_{xz} | $d_{x^2-y^2}$ |
|---------|-------------|----------------------------|-----------|-----------|-----------|----------|---------------|
| 1 | 0.000 | 0.0 | 0.911770 | 0.062704 | -0.110123 | 0.093734 | 0.379250 |
| 2 | 0.192 | 1552.5 | -0.077135 | 0.559466 | 0.180772 | 0.803458 | -0.053145 |
| 3 | 0.213 | 1716.7 | 0.061158 | -0.814403 | 0.022444 | 0.558393 | -0.143876 |
| 4 | 0.980 | 7907.2 | -0.386859 | -0.113348 | -0.048436 | 0.112672 | 0.906891 |
| 5 | 1.301 | 10492.0 | -0.096569 | 0.083455 | -0.975881 | 0.145505 | -0.100962 |

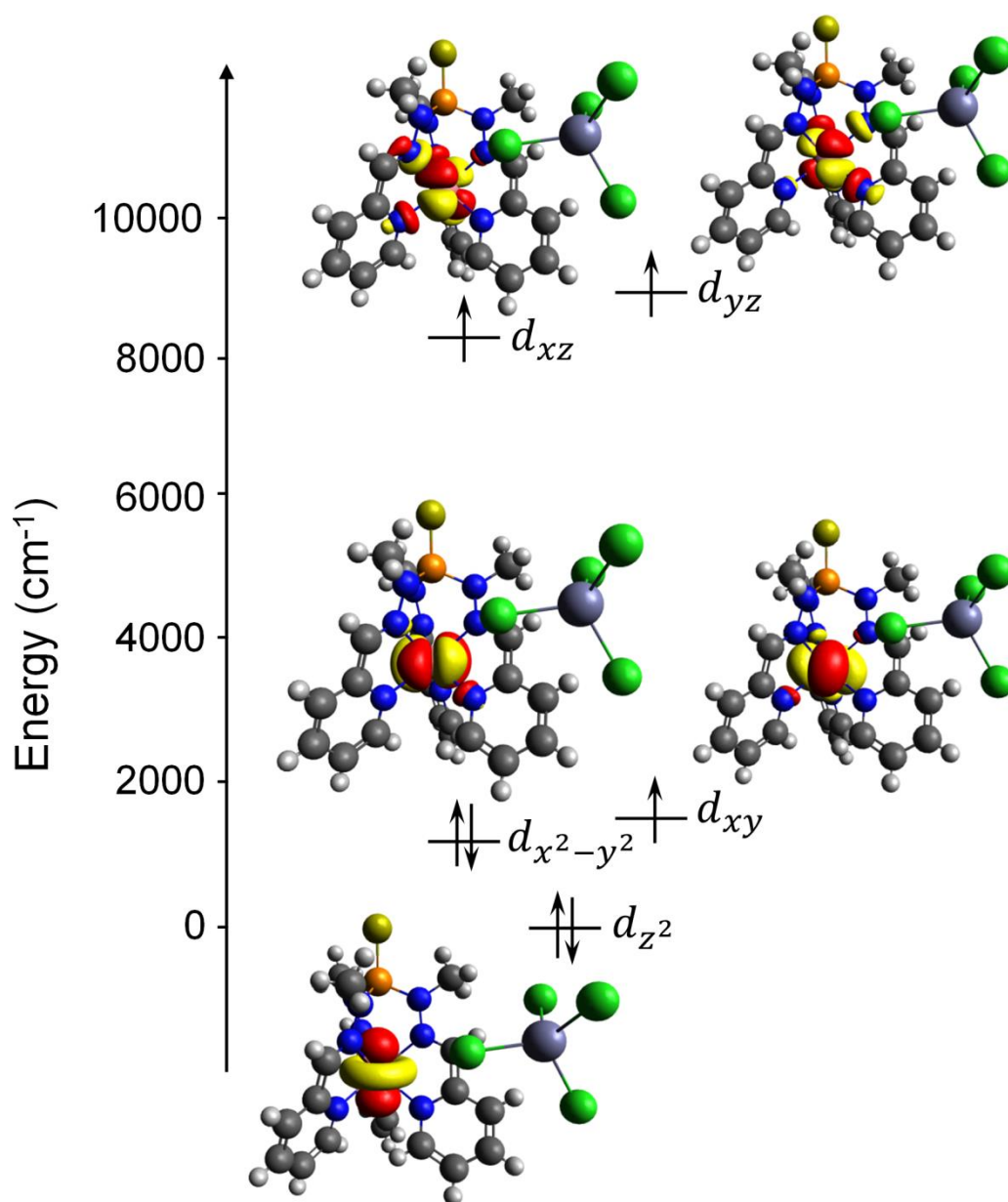
5 – NEVPT2

| Orbital | Energy (eV) | Energy (cm ⁻¹) | d_{xy} | d_{yz} | d_{z^2} | d_{xz} | $d_{x^2-y^2}$ |
|---------|-------------|----------------------------|-----------|-----------|-----------|-----------|---------------|
| 1 | 0.000 | 0.0 | 0.910723 | 0.075757 | -0.101916 | 0.103512 | 0.379135 |
| 2 | 0.180 | 1453.7 | -0.077412 | 0.894301 | 0.008277 | -0.422582 | 0.124854 |
| 3 | 0.190 | 1530.3 | -0.080806 | 0.419066 | 0.185261 | 0.881506 | -0.080500 |
| 4 | 1.059 | 8541.0 | -0.386778 | -0.108271 | -0.048135 | 0.109053 | 0.908004 |
| 5 | 1.368 | 11031.1 | -0.092003 | 0.084544 | -0.976169 | 0.147528 | -0.098576 |

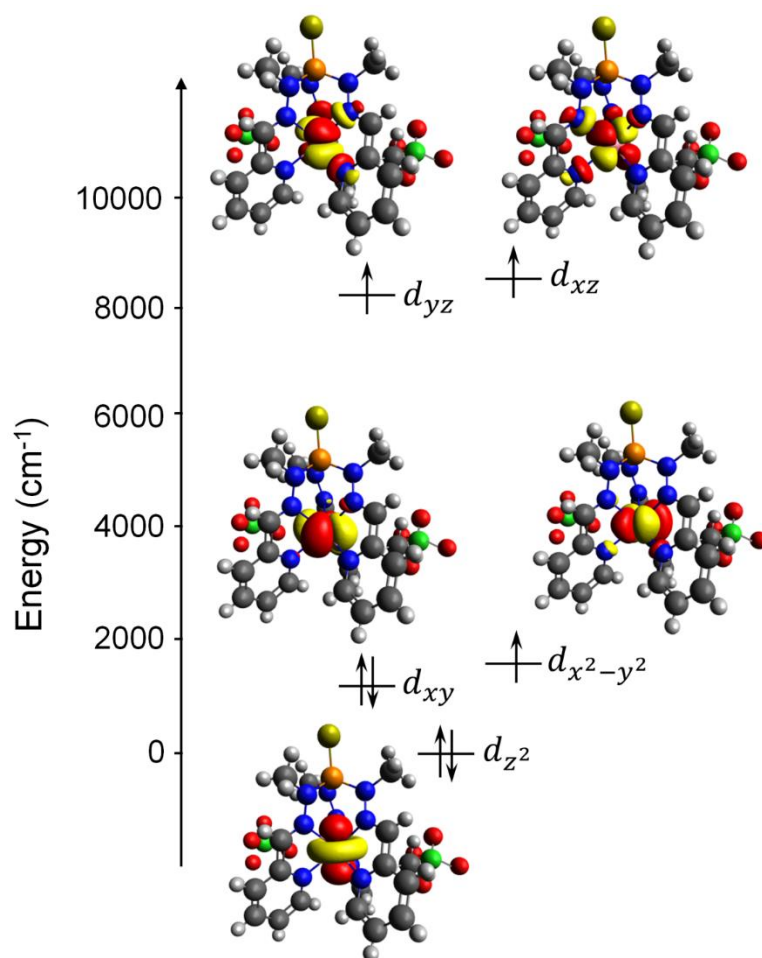
a) NEVPT2 Orbital energies for **1**: d_{z^2} : 0.0 cm⁻¹, d_{xy} : 949.1 cm⁻¹, $d_{x^2-y^2}$: 1565.9 cm⁻¹, d_{yz} : 9263.6 cm⁻¹, d_{xz} : 9493.5 cm⁻¹.



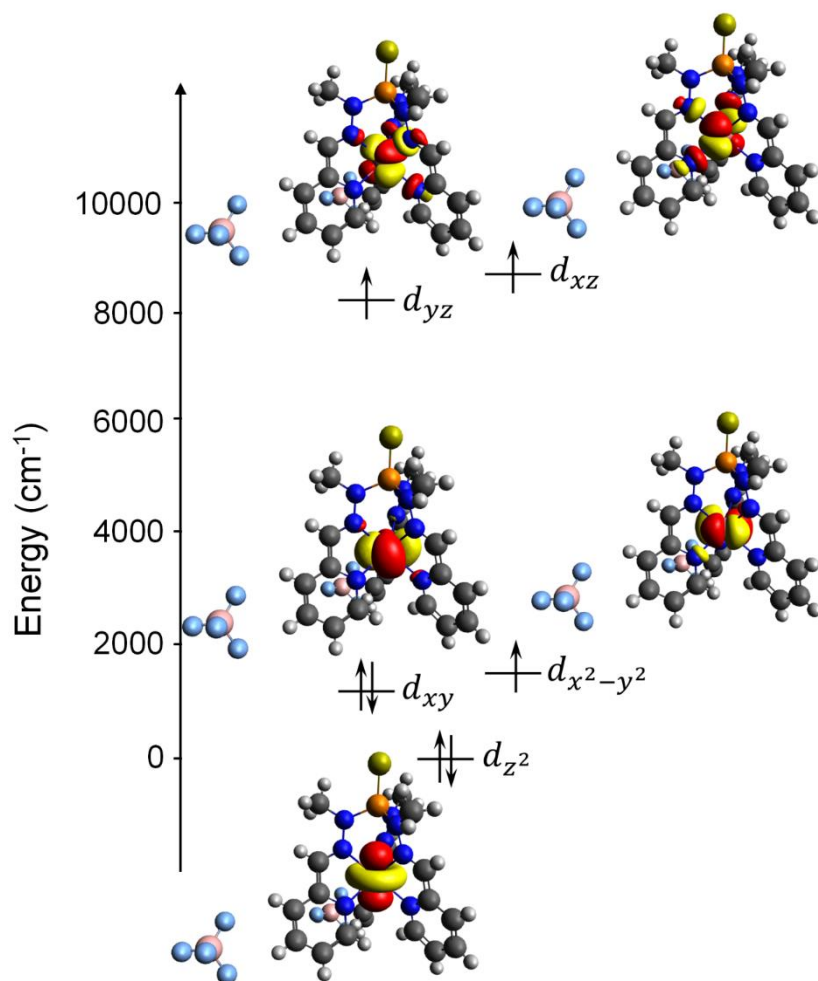
b) NEVPT2 Orbital energies for **2**: d_{z^2} : 0.0 cm^{-1} , $d_{x^2-y^2}$: 1071.6 cm^{-1} , d_{xy} : 1517.3 cm^{-1} , d_{xz} : 8227.0 cm^{-1} , d_{yz} : 8658.9 cm^{-1} .



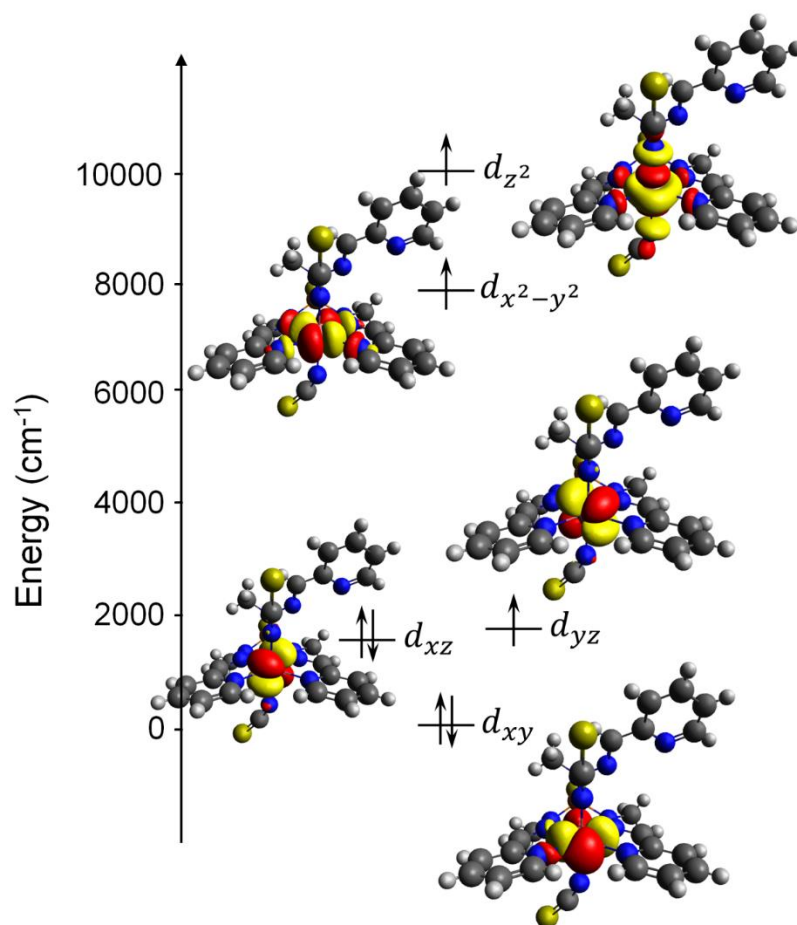
c) NEVPT2 Orbital energies for **3**: d_{z^2} : 0.0 cm^{-1} , d_{xy} : 1128.7 cm^{-1} , $d_{x^2-y^2}$: 1667.9 cm^{-1} , d_{yz} : 8099.9 cm^{-1} , d_{xz} : 8430.0 cm^{-1} .



d) NEVPT2 Orbital energies for **4**: d_{z^2} : 0.0 cm^{-1} , d_{xy} : 1114.8 cm^{-1} , $d_{x^2-y^2}$: 1538.8 cm^{-1} , d_{yz} : 8110.7 cm^{-1} , d_{xz} : 8559.4 cm^{-1} .



e) CASSCF Orbital energies for **5**: d_{xy} : 0.0 cm⁻¹, d_{xz} : 1552.5 cm⁻¹, d_{yz} : 1716.7 cm⁻¹, $d_{x^2-y^2}$: 7907.2 cm⁻¹, d_{z^2} : 10492.0 cm⁻¹.



NEVPT2 Orbital energies for **5**: d_{xy} : 0.0 cm^{-1} , d_{yz} : 1453.75 cm^{-1} , d_{xz} : 1530.3 cm^{-1} , $d_{x^2-y^2}$: 8541.0 cm^{-1} , d_{z^2} : 11031.1 cm^{-1} .

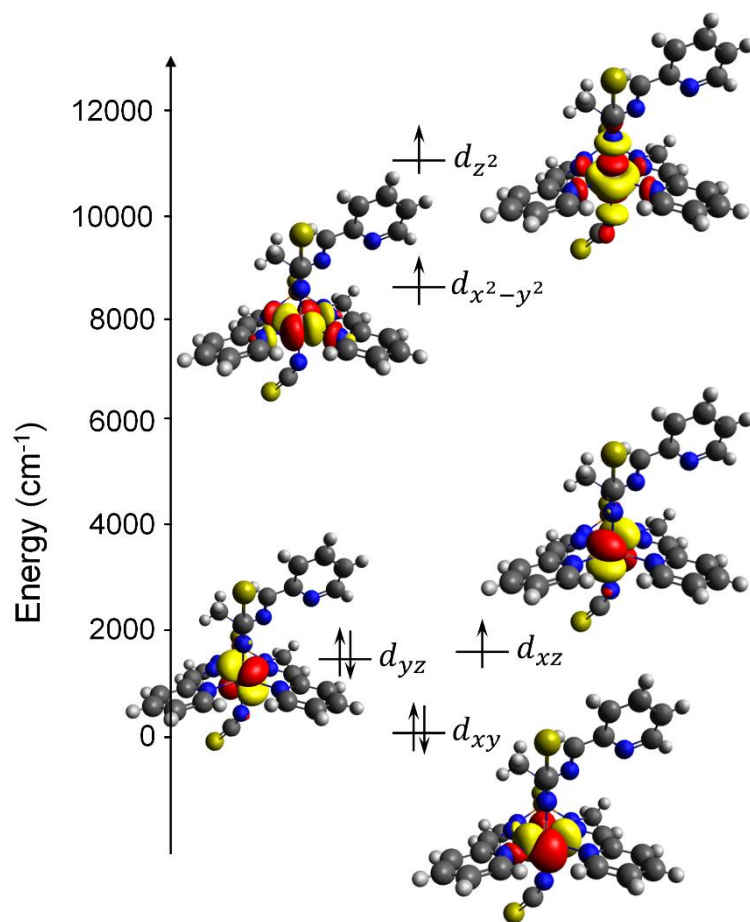


Figure S10.- AILFT computed d-orbital splitting for compounds **1** (a), **2** (b), **3** (c), **4** (d) and **5** (e).

Table S7: NEVPT2 computed electronic states, and the corresponding major electronic configurations. Note that minor contributions are not shown.

Complex 1

| Energy-CASCCF (cm ⁻¹) | Energy-NEVPT2 (cm ⁻¹) | Electronic configurations from CASSCF |
|--------------------------------------|--------------------------------------|--|
| 0 | 0 | $d_{xy}^2 d_{yz}^1 d_z^2 d_{xz}^1 d_{x^2-y^2}^1$ (91%) |
| 385.7 | 560.6 | $d_{xy}^1 d_{yz}^1 d_z^2 d_{xz}^1 d_{x^2-y^2}^2$ (93%) |
| 3465.8 | 4407.1 | $d_{xy}^1 d_{yz}^2 d_z^1 d_{xz}^1 d_{x^2-y^2}^2$ (22%) $d_{xy}^1 d_{yz}^2 d_z^1 d_{xz}^2 d_{x^2-y^2}^1$ (21%) $d_{xy}^2 d_{yz}^1 d_z^1 d_{xz}^1 d_{x^2-y^2}^2$ (21%) |
| 7653.3 | 10210.1 | $d_{xy}^2 d_{yz}^2 d_z^1 d_{xz}^1 d_{x^2-y^2}^1$ (42%) $d_{xy}^1 d_{yz}^1 d_z^2 d_{xz}^2 d_{x^2-y^2}^1$ (24%) |
| 7757.2 | 10464.8 | $d_{xy}^1 d_{yz}^2 d_z^2 d_{xz}^1 d_{x^2-y^2}^1$ (31%) $d_{xy}^1 d_{yz}^2 d_z^1 d_{xz}^1 d_{x^2-y^2}^2$ (25%) $d_{xy}^2 d_{yz}^1 d_z^1 d_{xz}^2 d_{x^2-y^2}^1$ (16%) |

Complex 2

| Energy-CASCCF (cm ⁻¹) | Energy-NEVPT2 (cm ⁻¹) | Electronic configurations from CASSCF |
|--------------------------------------|--------------------------------------|--|
| 0 | 0 | $d_{xy}^1 d_{yz}^1 d_z^2 d_{xz}^1 d_{x^2-y^2}^2$ (78%) $d_{xy}^2 d_{yz}^1 d_z^2 d_{xz}^1 d_{x^2-y^2}^1$ (16%) |
| 426.1 | 599.2 | $d_{xy}^2 d_{yz}^1 d_z^2 d_{xz}^1 d_{x^2-y^2}^1$ (79%) $d_{xy}^1 d_{yz}^1 d_z^2 d_{xz}^1 d_{x^2-y^2}^2$ (15%) |
| 3761.1 | 4823.3 | $d_{xy}^1 d_{yz}^2 d_z^1 d_{xz}^2 d_{x^2-y^2}^1$ (22%) $d_{xy}^2 d_{yz}^1 d_z^1 d_{xz}^1 d_{x^2-y^2}^2$ (19%) $d_{xy}^2 d_{yz}^2 d_z^1 d_{xz}^1 d_{x^2-y^2}^1$ (16%) |
| 6954.6 | 9223.4 | $d_{xy}^1 d_{yz}^1 d_z^1 d_{xz}^2 d_{x^2-y^2}^2$ (44%) $d_{xy}^1 d_{yz}^1 d_z^2 d_{xz}^2 d_{x^2-y^2}^1$ (33%) |
| 7150.9 | 9685.2 | $d_{xy}^1 d_{yz}^2 d_z^2 d_{xz}^1 d_{x^2-y^2}^1$ (39%) $d_{xy}^1 d_{yz}^2 d_z^1 d_{xz}^1 d_{x^2-y^2}^2$ (29%) |

Complex 3

| Energy-CASCCF (cm ⁻¹) | Energy-NEVPT2 (cm ⁻¹) | Electronic configurations from CASSCF |
|--------------------------------------|--------------------------------------|--|
| 0 | 0 | $d_{xy}^2 d_{yz}^1 d_z^2 d_{xz}^1 d_{x^2-y^2}^1$ (89%) |
| 320.6 | 450.6 | $d_{xy}^1 d_{yz}^1 d_z^2 d_{xz}^1 d_{x^2-y^2}^2$ (88%) |
| 3974.6 | 5118.5 | $d_{xy}^2 d_{yz}^2 d_z^1 d_{xz}^1 d_{x^2-y^2}^1$ (29%) $d_{xy}^1 d_{yz}^1 d_z^1 d_{xz}^2 d_{x^2-y^2}^2$ (28%) $d_{xy}^1 d_{yz}^2 d_z^1 d_{xz}^2 d_{x^2-y^2}^1$ (21%) |

| | | |
|--------|--------|--|
| 6704.4 | 8942.4 | $d_{xy}^2 d_{yz}^1 d_z^2 d_{xz}^2 d_{x^2-y^2}^1$ (31%) $d_{xy}^1 d_{yz}^1 d_z^2 d_{xz}^2 d_{x^2-y^2}^1$ (22%) $d_{xy}^2 d_{yz}^2 d_z^2 d_{xz}^1 d_{x^2-y^2}^1$ (19%) |
| 7011.9 | 9931.8 | $d_{xy}^1 d_{yz}^2 d_z^2 d_{xz}^1 d_{x^2-y^2}^1$ (28%) $d_{xy}^1 d_{yz}^2 d_z^2 d_{xz}^1 d_{x^2-y^2}^2$ (22%) $d_{xy}^1 d_{yz}^1 d_z^2 d_{xz}^2 d_{x^2-y^2}^1$ (14%) |

Complex 4

| Energy-CASCCF (cm^{-1}) | Energy-NEVPT2 (cm^{-1}) | Electronic configurations from CASSCF |
|---------------------------------------|---------------------------------------|--|
| 0 | 0 | $d_{xy}^2 d_{yz}^1 d_z^2 d_{xz}^1 d_{x^2-y^2}^1$ (71%) $d_{xy}^1 d_{yz}^1 d_z^2 d_{xz}^1 d_{x^2-y^2}^2$ (23%) |
| 303.7 | 426.8 | $d_{xy}^1 d_{yz}^1 d_z^2 d_{xz}^1 d_{x^2-y^2}^2$ (71%) $d_{xy}^2 d_{yz}^1 d_z^2 d_{xz}^1 d_{x^2-y^2}^1$ (24%) |
| 3971.0 | 5086.1 | $d_{xy}^2 d_{yz}^1 d_z^2 d_{xz}^2 d_{x^2-y^2}^1$ (25%) $d_{xy}^1 d_{yz}^2 d_z^2 d_{xz}^1 d_{x^2-y^2}^2$ (24%) $d_{xy}^1 d_{yz}^2 d_z^2 d_{xz}^2 d_{x^2-y^2}^1$ (21%) |
| 6922.6 | 9302.7 | $d_{xy}^2 d_{yz}^2 d_z^2 d_{xz}^1 d_{x^2-y^2}^1$ (42%) $d_{xy}^1 d_{yz}^1 d_z^2 d_{xz}^2 d_{x^2-y^2}^1$ (34%) |
| 7061.2 | 9443.8 | $d_{xy}^1 d_{yz}^2 d_z^2 d_{xz}^1 d_{x^2-y^2}^1$ (37%) $d_{xy}^1 d_{yz}^2 d_z^2 d_{xz}^1 d_{x^2-y^2}^2$ (27%) |

Complex 5

| Energy-CASCCF (cm^{-1}) | Energy-NEVPT2 (cm^{-1}) | Electronic configurations from CASSCF |
|---------------------------------------|---------------------------------------|--|
| 0 | 0 | $d_{xy}^2 d_{yz}^2 d_z^2 d_{xz}^1 d_{x^2-y^2}^1$ (55%) $d_{xy}^2 d_{yz}^1 d_z^2 d_{xz}^2 d_{x^2-y^2}^1$ (16%) |
| 1021.5 | 1346.9 | $d_{xy}^2 d_{yz}^1 d_z^2 d_{xz}^2 d_{x^2-y^2}^1$ (58%) $d_{xy}^2 d_{yz}^2 d_z^2 d_{xz}^1 d_{x^2-y^2}^1$ (17%) |
| 1584.2 | 2148.1 | $d_{xy}^1 d_{yz}^2 d_z^2 d_{xz}^2 d_{x^2-y^2}^1$ (76%) |
| 7674.6 | 10182.6 | $d_{xy}^1 d_{yz}^2 d_z^2 d_{xz}^1 d_{x^2-y^2}^2$ (42%) $d_{xy}^1 d_{yz}^1 d_z^2 d_{xz}^2 d_{x^2-y^2}^2$ (17%) $d_{xy}^1 d_{yz}^2 d_z^2 d_{xz}^1 d_{x^2-y^2}^1$ (17%) |
| 7991.6 | 10477.1 | $d_{xy}^1 d_{yz}^1 d_z^2 d_{xz}^2 d_{x^2-y^2}^2$ (50%) $d_{xy}^1 d_{yz}^1 d_z^2 d_{xz}^2 d_{x^2-y^2}^1$ (21%) |

Table S8: Contributions to D -tensor from NEVPT2 calculations (except for **5**, for which CASSCF and NEVPT2 results are given).

| | 1 | | 2 | |
|--------------|-------------------|---------|-------------------|---------|
| | D | E | D | E |
| ${}^4\Phi_1$ | -108.191 | -0.009 | -109.186 | -0.019 |
| ${}^4\Phi_2$ | 5.115 | -5.101 | 4.859 | -4.860 |
| ${}^4\Phi_3$ | 4.684 | 5.195 | 5.968 | 5.896 |
| ${}^4\Phi_4$ | 2.214 | -3.560 | 2.532 | -3.659 |
| ${}^4\Phi_5$ | 0.200 | 0.154 | 0.288 | 0.314 |
| | 3 | | 4 | |
| | D | E | D | E |
| ${}^4\Phi_1$ | -125.044 | -0.012 | -127.417 | -0.008 |
| ${}^4\Phi_2$ | 4.032 | -4.026 | 4.524 | -4.539 |
| ${}^4\Phi_3$ | 6.083 | 5.879 | 3.537 | -0.218 |
| ${}^4\Phi_4$ | 2.283 | -3.579 | 4.330 | 1.816 |
| ${}^4\Phi_5$ | 0.502 | 0.347 | 0.887 | 0.899 |
| | 5 - CASSCF | | 5 - NEVPT2 | |
| | D | E | D | E |
| ${}^4\Phi_1$ | 32.818 | 32.791 | -52.682 | -0.016 |
| ${}^4\Phi_2$ | 20.467 | -20.447 | 15.479 | -15.503 |
| ${}^4\Phi_3$ | 0.995 | 1.005 | -1.511 | 0.002 |
| ${}^4\Phi_4$ | 4.356 | 4.504 | -6.847 | 0.056 |
| ${}^4\Phi_5$ | -13.908 | 0.022 | 5.319 | 5.347 |

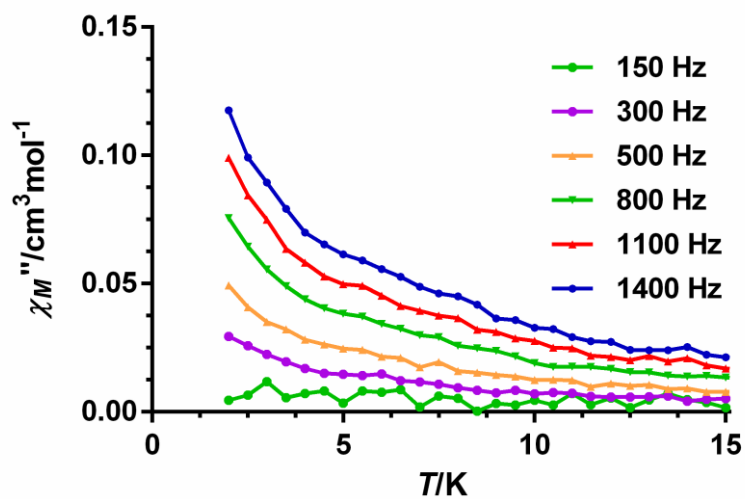


Figure S11.- Temperature dependence of χ_M'' for compound **2** at the indicated frequencies at zero dc field. Solid lines are only a guide for the eye.

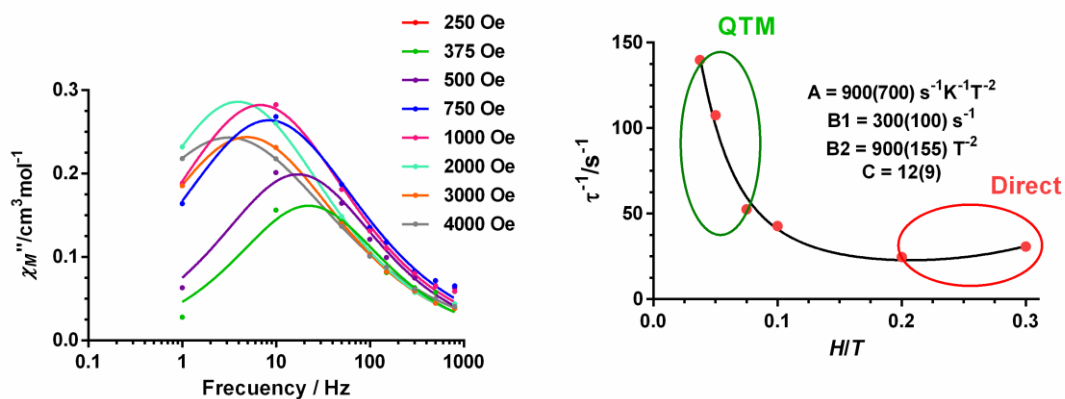


Figure S12.- (Left) Frequency dependence of χ_M'' for compound **2** at 2 K and at the indicated fields. Solid lines are the best fits to the generalized Debye model. (Right) Field dependence of the relaxation times for **2**. The solid line represents the best fit to the indicated equation.

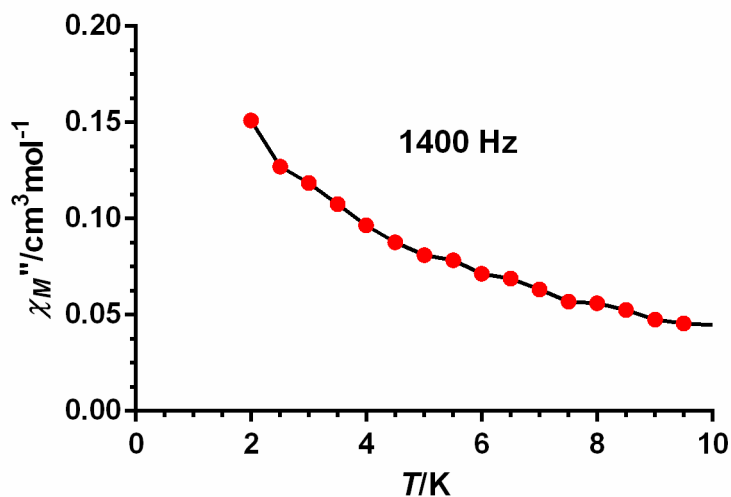


Figure S13.- Temperature dependence of χ_M'' for compound **3** at 1400 Hz and zero dc field. The solid line is only a guide for the eye.

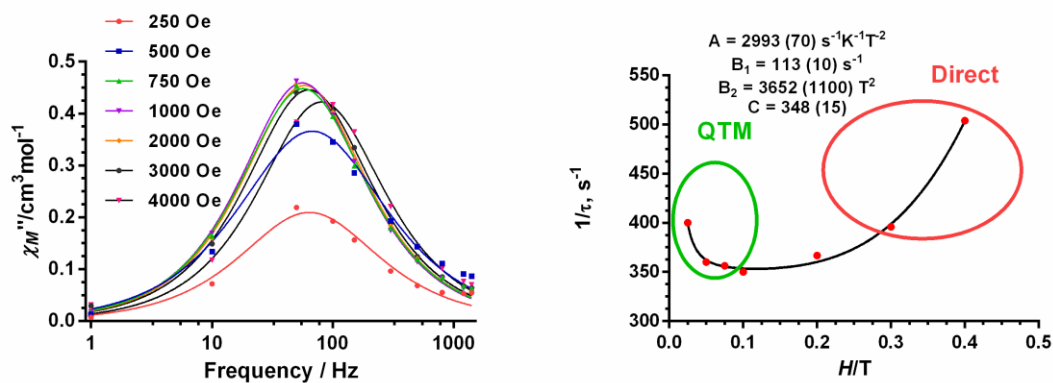


Figure S14.- (Left) Field dependence of χ_M'' for compound **3** at 2 K. Solid lines are the best fits to the generalized Debye model. (Right) Field dependence of the relaxation times for **3**. The solid line represents the best fit to the equation 1.

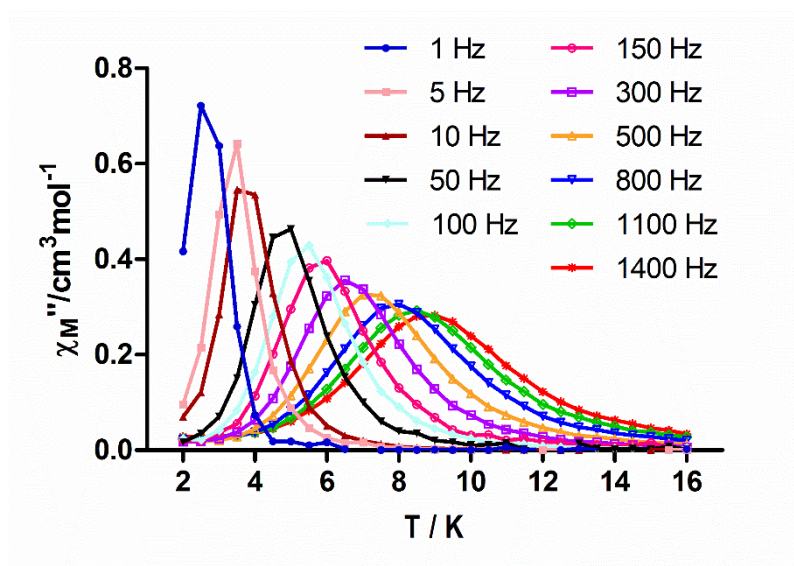


Figure S15.- Temperature dependence of χ_M'' for compound **3** at the indicated frequencies and at applied dc field 0.1 T. Solid lines are only a guide for the eye.

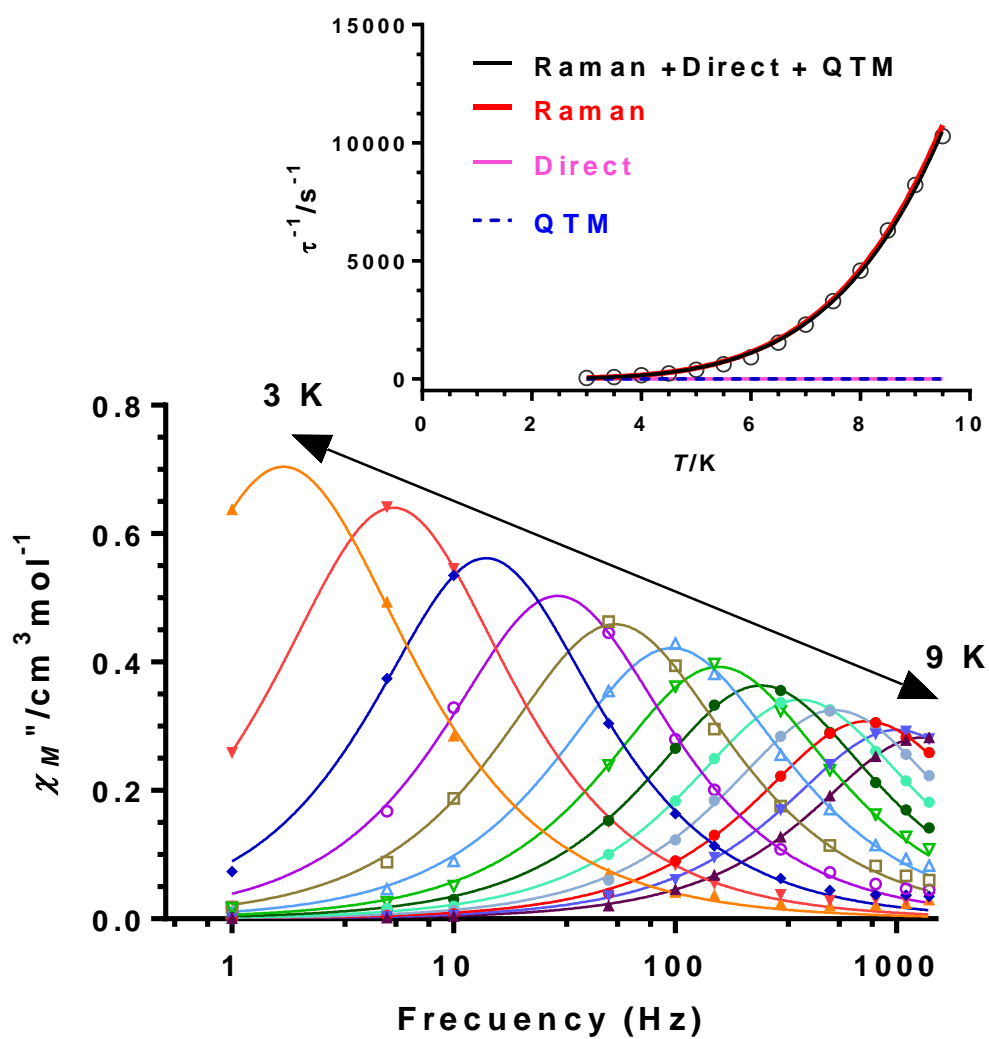


Figure S16.- Frequency dependence of χ''_M at different frequencies and temperature dependence of the relaxation time τ^{-1} (inset) for complex **3**. Contribution of each of the relaxation process to the slow relaxation of the magnetization of **3** (inset).

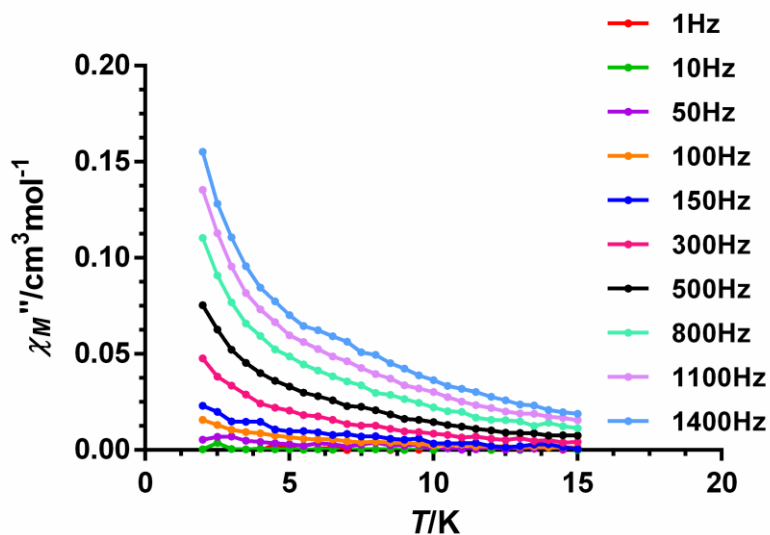


Figure S17.- Temperature dependence of χ_M'' for compound **4** at the indicated frequencies at zero dc field. Solid lines are only a guide for the eye.

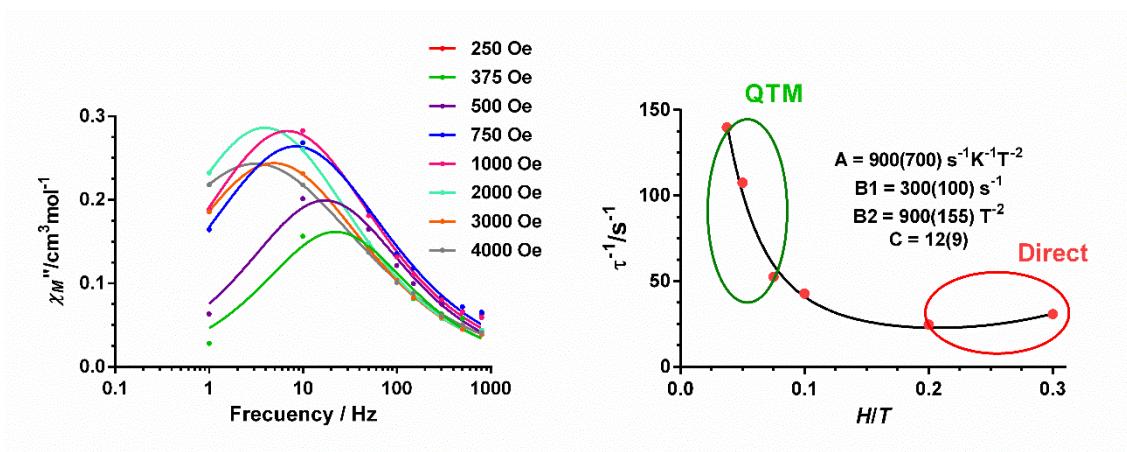


Figure S18.- (Left) Field dependence of χ_M'' for compound **4** at 2 K. Solid lines are the best fits to the generalized Debye model. (Right) Field dependence of the relaxation times for **4**. The solid line represents the best fit to the equation 3.

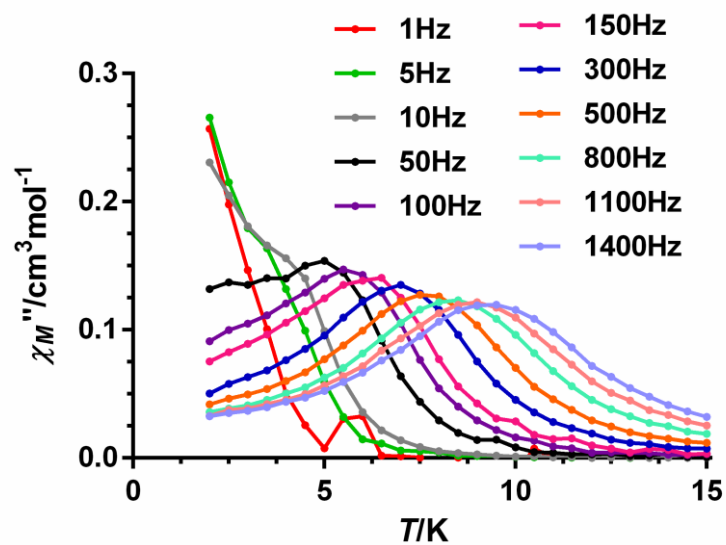


Figure S19.- Temperature dependence of χ''_M for compound **4** at the indicated frequencies and at applied dc field 0.2 T. Solid lines are only a guide for the eye.

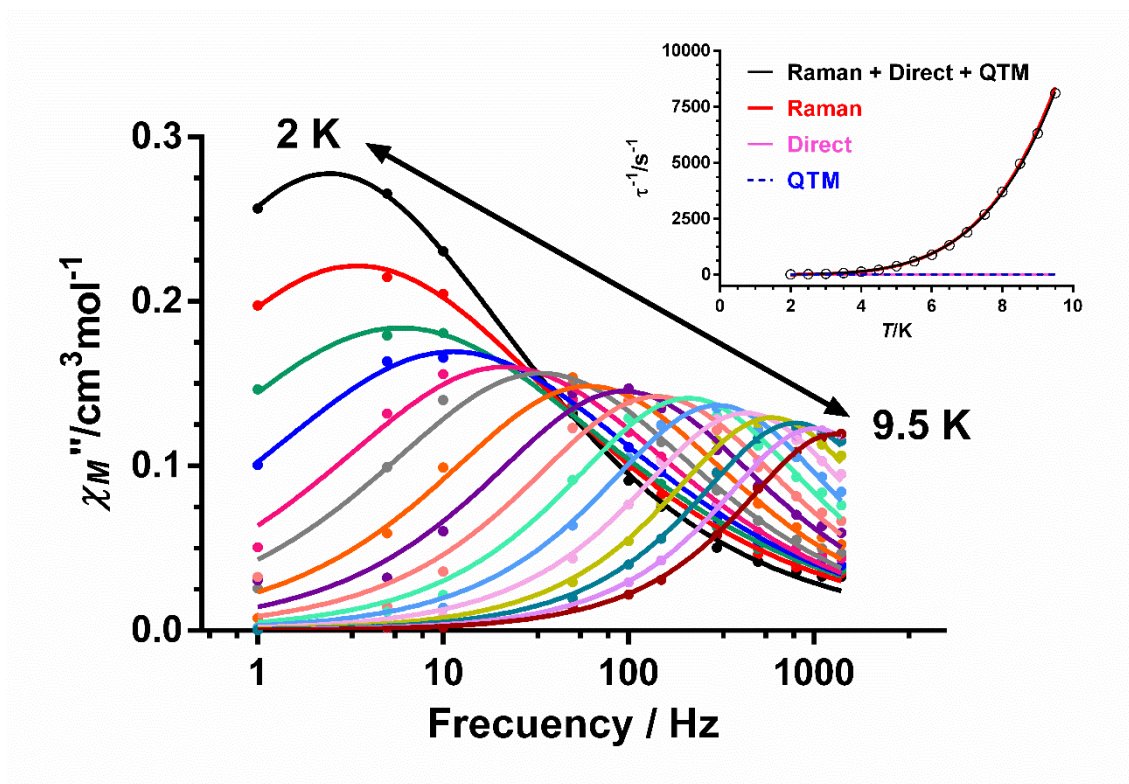


Figure S20.- Frequency dependence of χ''_M at different frequencies (left) and frequency dependence of at different temperatures (right) for **4**. Contribution of each relaxation process to the slow relaxation of the magnetization of **4** (inset).

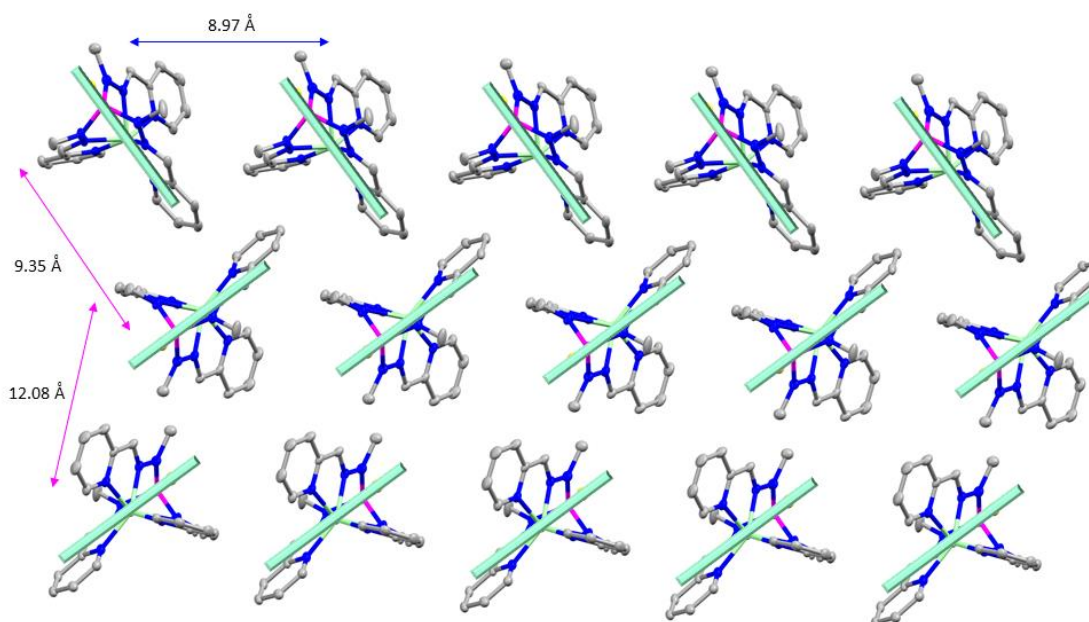


Figure S21.- Orientation of the anisotropy axes for the shortest Co···Co distance in the crystal packing of **3**.

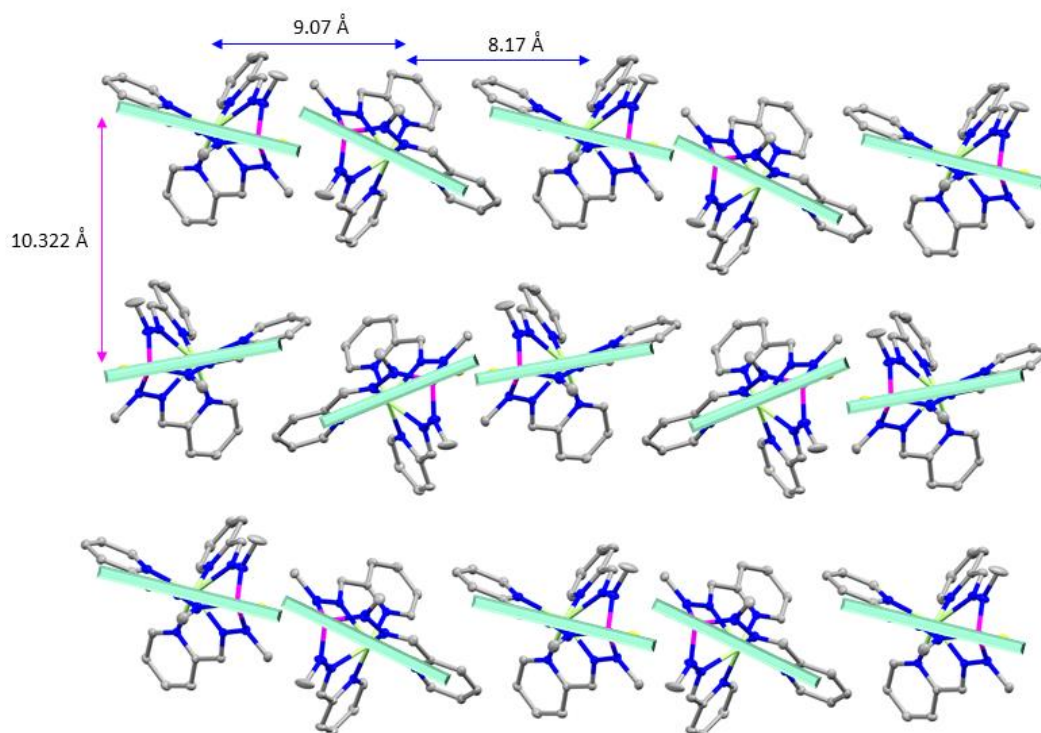


Figure S22.- Orientation of the anisotropy axes for the shortest Co···Co distance in the crystal packing of **2**.

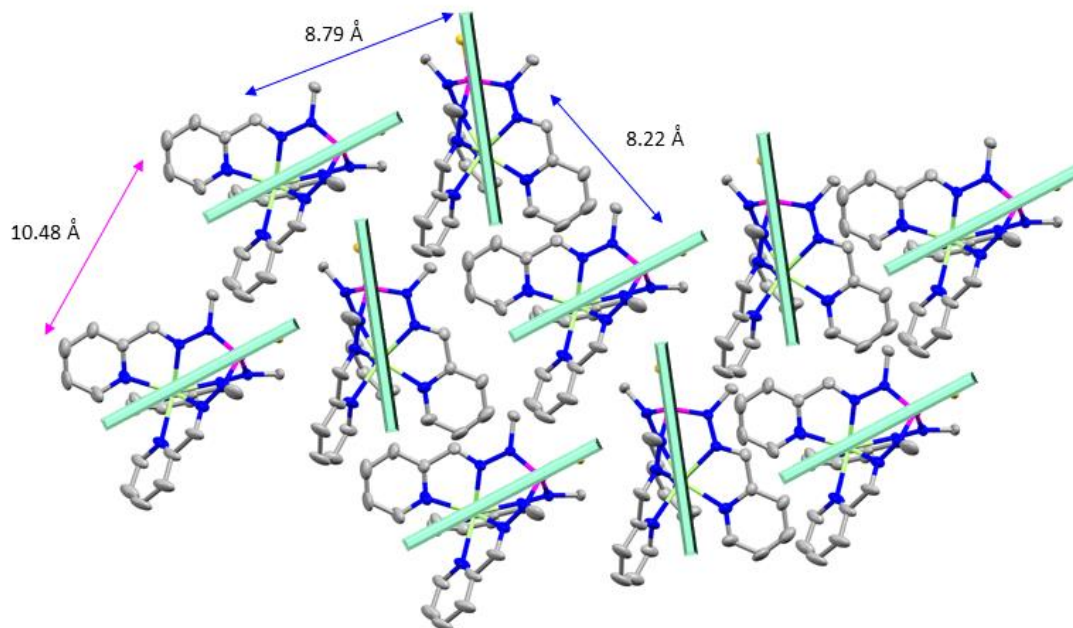


Figure S23.- Orientation of the anisotropy axes for the shortest Co...Co distance in the crystal packing of **4**.

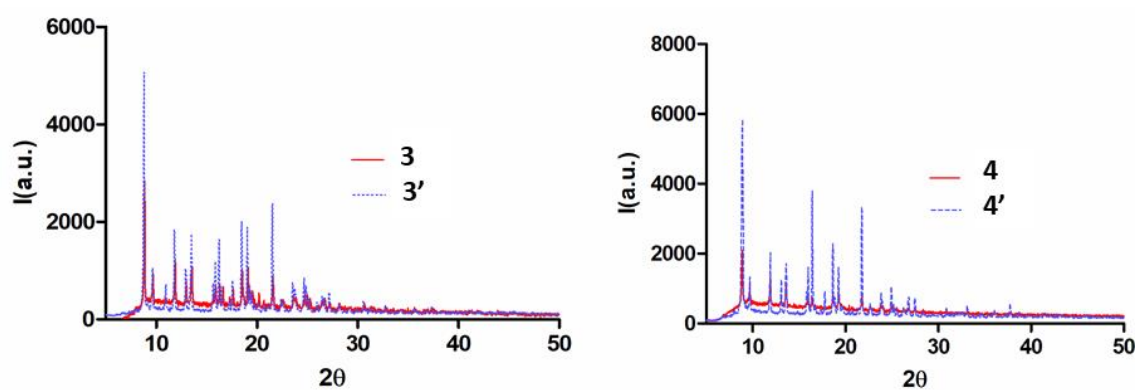


Figure S24.- Powder XRD spectra **3** and **3'** (left) and **4** and **4'** (right)

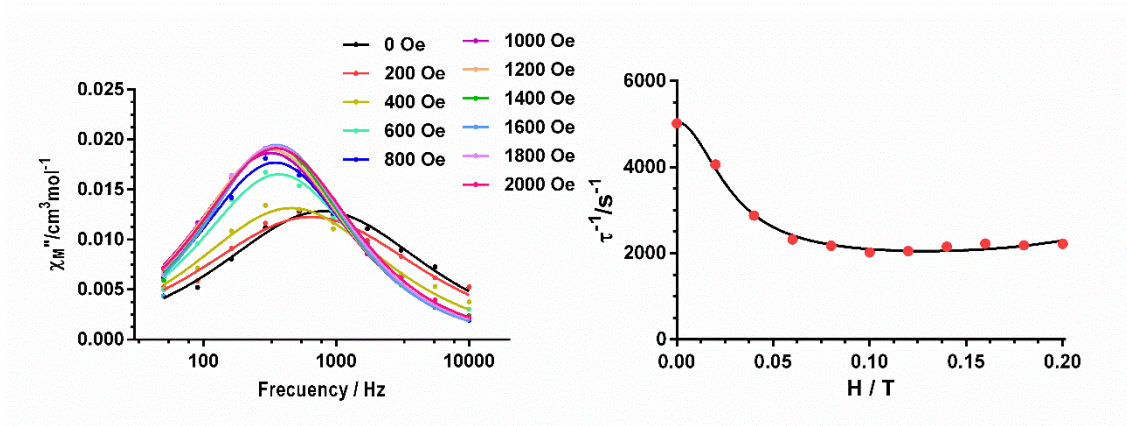


Figure S25. - (Left) Field dependence of χ_M'' for compound **3'** at 7K. The solid lines are the best fits to the generalized Debye model. (Right) Field dependence of the relaxation times for **3'**. The solid line represents the best fit to the equation 3.

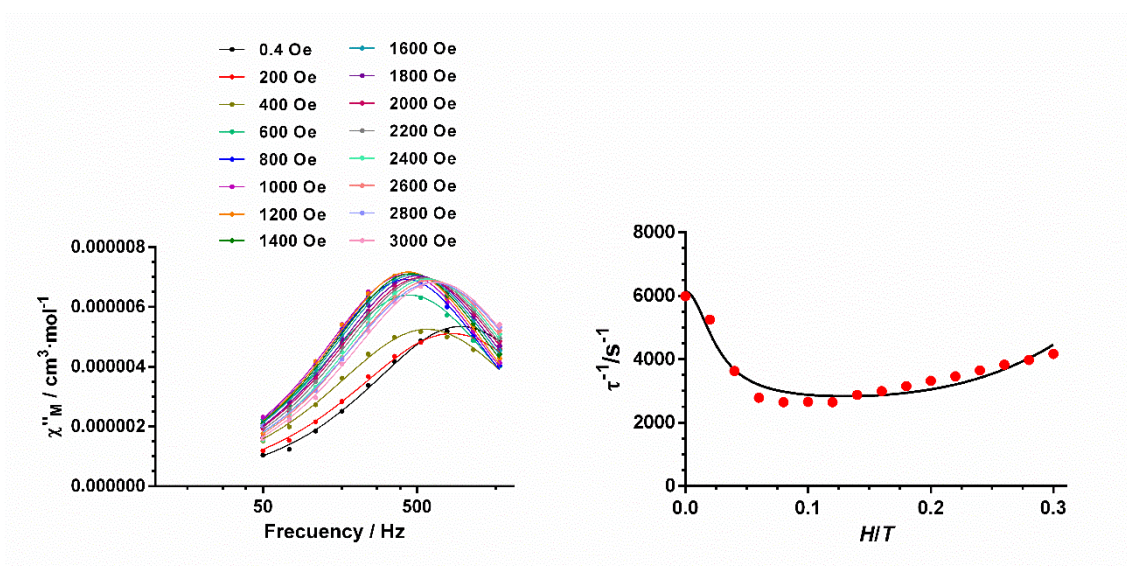


Figure S26. - (Left) Field dependence of χ_M'' for compound **4'** at 7K. The solid lines are the best fits to the generalized Debye model. (Right) Field dependence of the relaxation times for **4'**. The solid line represents the best fit to the equation 3.

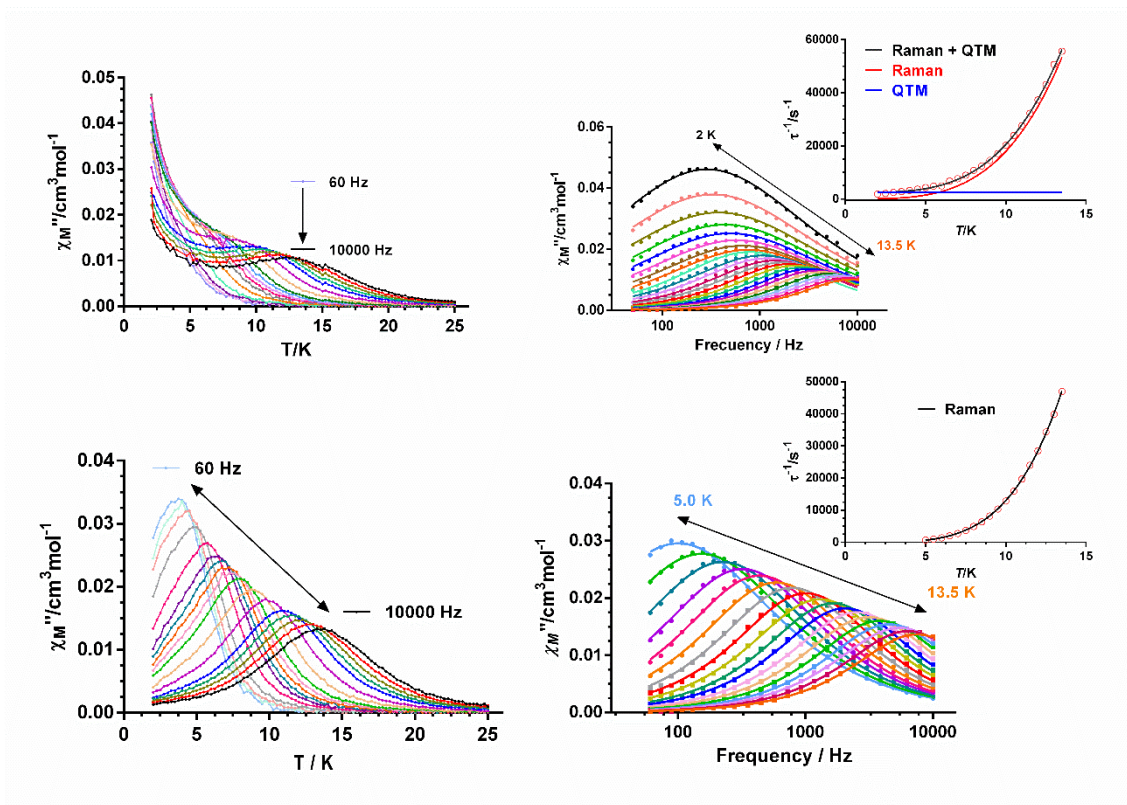


Figure S27.- Temperature dependence of χ''_M at different frequencies for $4'$ at zero field (top left) and at 0.12 T (bottom left) and frequency dependence of the relaxation time τ at different temperatures for complex $4'$ at zero field (top right) and at 0.12 T (bottom right). The black lines represent the best fit of the experimental data to a combination of Raman and QTM processes (inset top right) and to Raman process (inset bottom right). Red and blue solid lines correspond to the Raman and QTM contributions to the magnetization relaxation, respectively.

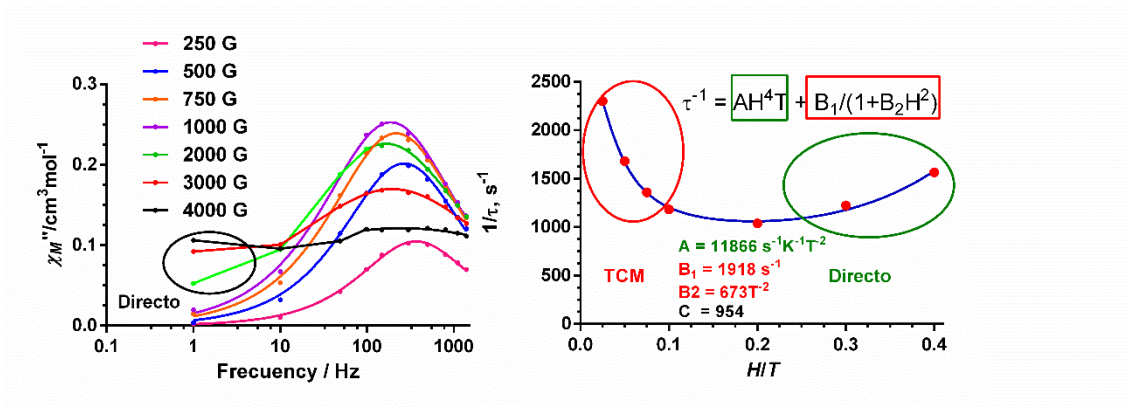


Figure S28.- (Left) Field dependence of χ_M'' for compound **5** at 2 K. The solid lines are the best fits to the generalized Debye model. (Right) Field dependence of the relaxation times for **5**. The solid line represents the best fit to the equation 3.

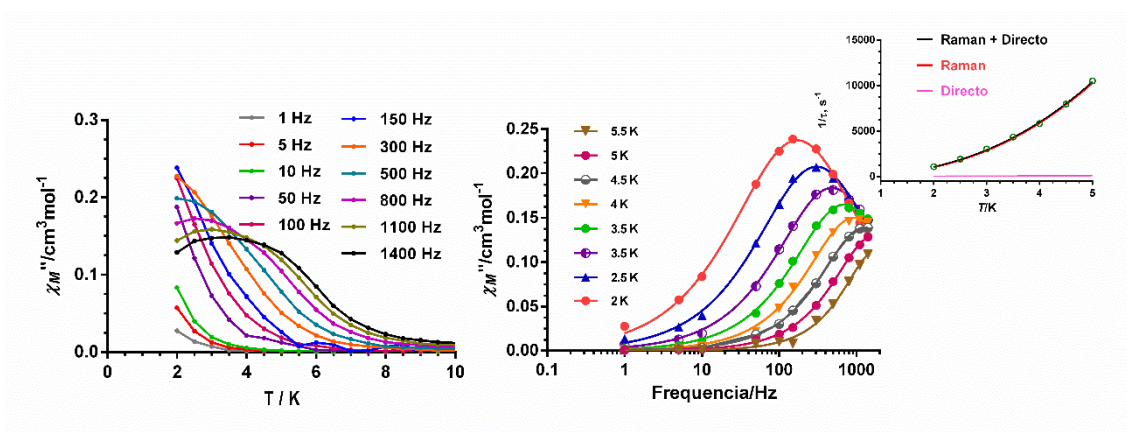


Figure S29.- (Left) Temperature dependence of χ_M'' at different frequencies for **5** at 0.2 T. Temperature dependence of the relaxation time τ for complex **5**. The blue and green lines represent the best fits of the experimental data to the Arrhenius equation for a thermally activated process and to a combination of Raman and direct processes, respectively. (Right) Frequency dependence of χ_M'' at different temperatures for **5** at 0.2 T.

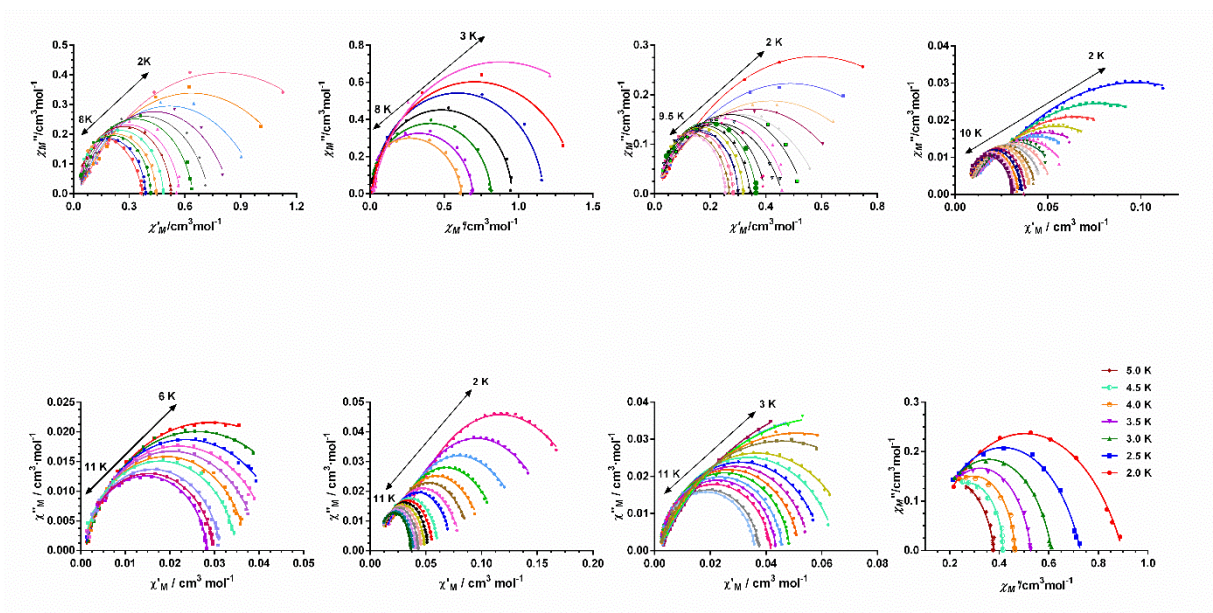


Figure S30.- Cole-Cole diagrams for **2**, **3**, **4** under the optimal field and **3'** under zero field (top, from left to right) and **3'** under the optimal field, and **4'** under zero field, **4'** under the optimal field, and **5** under the optimal field.

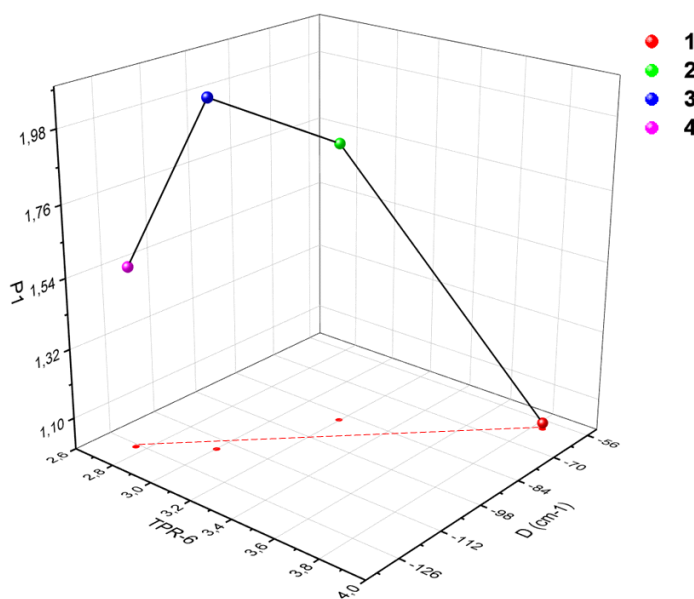


Figure S31.-3D plot of the position of the P1 peak of the hysteresis loop as a function of the axial anisotropy parameter versus the continuous symmetry measures for the TPR-6 complexes **1-4**. The red discontinuous solid line represents the best linear fitting of D vs continuous shape measures leading to the equation $D = 63 \cdot S(\text{TPR-6}) - 300$.

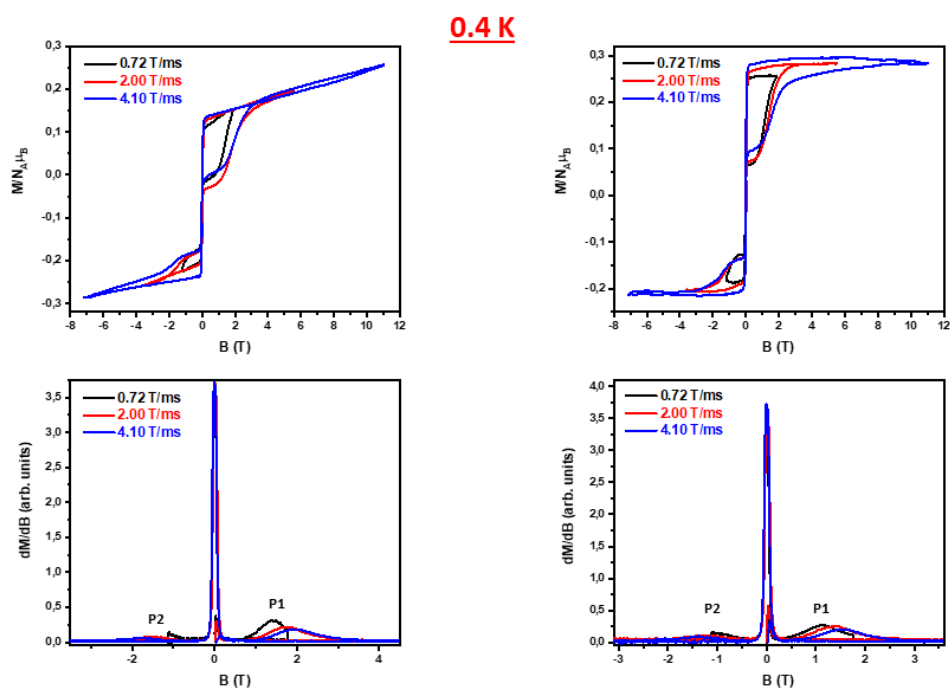


Figure S32.- Pulse magnetization at 0.4 K for 3' (left top) and 4' (right top) and field dependence of the differential magnetization for 3' (left bottom) and 4' (right bottom).

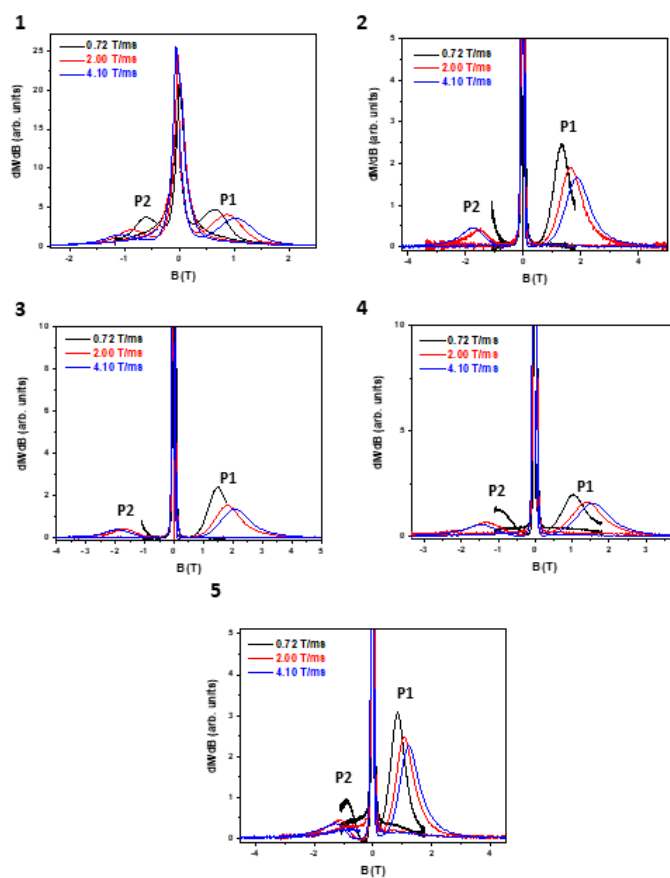


Figure S33.- Field dependence of the differential magnetization for compounds 1-5.

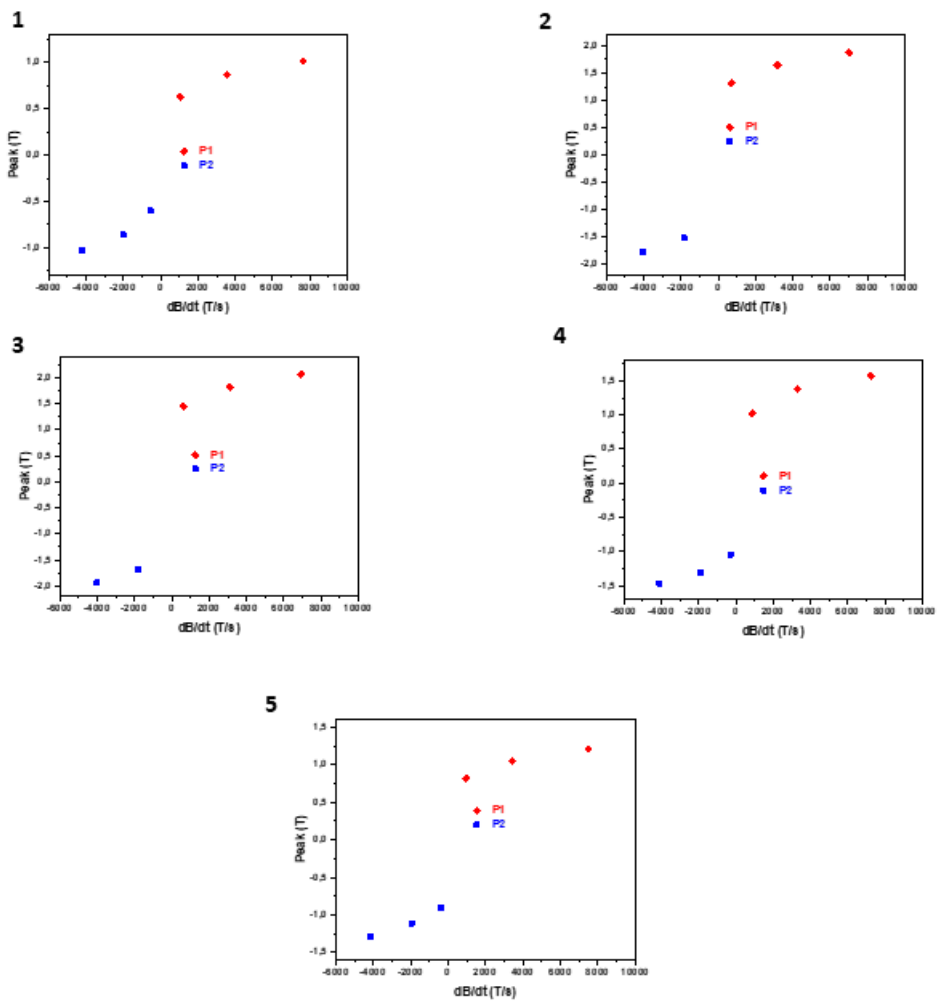


Figure 34.- Sweep rate dependence of peaks P1-P2 for compounds 1-5.

Table S10: Crystallographic data and structural refinement details for complexes **1-5**.

| Compound | 1 | 2 | 3 | 4 | 5 |
|--|---|--|---|--|---|
| Formula | C ₂₃ H ₂₇ Cl ₄ Co ₂ N ₁₀ PS | C ₂₂ H ₂₇ Cl ₄ CoN ₉ O _{0.95} PSZn | C _{22.68} H _{30.05} Cl ₂ Co N ₉ O _{9.35} PS | C ₂₁ H ₂₄ B ₂ CoF ₈ N ₉ PS | C ₂₃ H ₂₅ CoN ₁₁ PS ₃ |
| M_r | 766.23 | 761.85 | 771.25 | 698.07 | 641.62 |
| Crystal System | orthorhombic | orthorhombic | monoclinic | monoclinic | monoclinic |
| Space Group | P2 ₁ 2 ₁ 2 ₁ | Fdd2 | P2 ₁ /n | Cc | P2 ₁ /c |
| a (Å) | 10.6275(3) | 30.9259(16) | 8.9742(8) | 12.3914(7) | 14.6839(6) |
| b (Å) | 13.1662(4) | 40.000(2) | 32.745(3) | 25.9747(14) | 12.8377(5) |
| c (Å) | 21.7874(6) | 10.1498(5) | 10.9213(10) | 10.4816(6) | 15.6893(6) |
| α (°) | 90 | 90 | 90 | 90 | 90 |
| β (°) | 90 | 90 | 103.079(2) | 120.883(2) | 109.5797(14) |
| γ (°) | 90 | 90 | 90 | 90 | 90 |
| V (Å³) | 3048.58(15) | 12555.8(11) | 3126.1(5) | 2895.3(3) | 2786.53(19) |
| Z | 4 | 16 | 4 | 4 | 4 |
| D_c (g cm⁻³) | 1.669 | 1.612 | 1.639 | 1.601 | 1.529 |
| μ(MoK_α) (mm⁻¹) | 1.594 | 1.784 | 0.904 | 0.803 | 0.935 |
| T (K) | 100(2) | 100(2) | 100(2) | 100(2) | 100(2) |
| Observed reflections^a | 7899 (7705) | 9117 (8833) | 8032 (7534) | 6643 (6262) | 6916 (5671) |
| R_{int}^a | 0.0224 (0.0222) | 0.0439 (0.0386) | 0.0272 (0.0236) | 0.0533 (0.0244) | 0.0454 (0.0350) |
| Parameters | 374 | 367 | 432 | 392 | 365 |
| GOF | 1.087 | 0.694 | 1.629 | 1.391 | 0.921 |
| R₁^{b,a} | 0.0182 (0.0175) | 0.0289 (0.0279) | 0.0485 (0.0457) | 0.0589 (0.0553) | 0.0472 (0.0332) |
| wR₂^{c,a} | 0.0438 (0.0435) | 0.0830 (0.0807) | 0.1841 (0.1807) | 0.1750 (0.1698) | 0.1200 (0.1061) |
| ^a Values in parentheses for reflections with I > 2σ(I) ^b $R_1 = \sum F_o - F_c / \sum F_o $ ^c $wR_2 = \{ \sum [w(F_o^2 - F_c^2)^2] / \sum [w(F_o^2)^2] \}^{1/2}$ | | | | | |

References

- 23.- M.W. Löble, M. Casimiro, D. T. Thielemann, P. Oña-Burgos, I. Fernandez, P.W. Roesky, F. Breher, 1H,89YHMQC and Further NMR Spectroscopic and X-ray Diffraction Investigations on Yttrium-Containing Complexes Exhibiting Various Nuclearities. *Chem. Eur. J.* 2012, **18**, 5325–5334.
- 24.- S. Stoll and A. Schweiger, EasySpin, a comprehensive software package for spectral simulation and analysis in EPR, *J. Magn. Reson.*, 2006, **178**, 42-55.
- 25.- APEX2, Bruker AXS, Madison, WI, 2010.
- 26.- SAINT, Version 8.30a, Bruker AXS, Madison, WI, 2013.
- 27.- G. M. Sheldrick, SADABS, Version 2004/1, Bruker AXS, Madison, WI, 2008.
- 28.- O. V. Dolomanov, L. J. Bourhis, R. J. Gildea, J. A. K. Howard, H. Pushman, OLEX2: A complete structure solution, refinement and analysis program. *J. Appl. Crystallogr.*, 2009, **42**, 339-341.
- 29.- P. A. Malmqvist, B. O. Roos, The CASSCF state interaction method. *Chem. Phys. Lett.* 1989, **155**, 189–194.
- 30.- (a) C. Angeli, R. Cimiraglia, J.-P. Malrieu, N-electron valence state perturbation theory: a fast implementation of the strongly contracted variant. *Chem. Phys. Lett.* 2001, **350**, 297–305. (b) C. Angeli, R. Cimiraglia, S. Evangelisti, T. Leininger, J.-P. Malrieu, Introduction of n-electron valence states for multireference perturbation theory. *J. Chem. Phys.* 2001, **114**, 10252–10264. (c) C. Angeli, R. Cimiraglia, J.-P. Malrieu, N-electron valence state perturbation theory: A spinless formulation and an efficient implementation of the strongly contracted and of the partially contracted variants. *J. Chem. Phys.* 2002, **117**, 9138–9153.
- 31.- (a) F. Weigend and R. Ahlrichs, Balanced basis sets of split valence, triple zeta valence and quadruple zeta valence quality for H to Rn: Design and assessment of accuracy, *Phys. Chem. Chem. Phys.*, 2005, **7**, 3297-3305; (b) A. Schaefer, H. Horn and R. Ahlrichs, Fully optimized contracted Gaussian basis sets for atoms Li to Kr, *J. Chem. Phys.*, 1992, **97**, 2571-2577; (c) A. Schaefer, C. Huber and R. Ahlrichs, Fully optimized contracted Gaussian basis sets of triple zeta valence quality for atoms Li to Kr, *J. Chem. Phys.*, 1994, **100**, 5829-5835.
- 32.- F. Neese, "Software update: The ORCA program system, version 4.0". Wiley Interdisciplinary Reviews: Computational Molecular Science, 2018, **8**, e1327
- 33.- (a) D. Ganyushin and F. Neese, A fully variational spin-orbit coupled complete active space self-consistent field approach: Application to electron paramagnetic resonance g-tensors, *J. Chem. Phys.*, 2013, **138**, 104113; (b) D. Ganyushin and F. Neese, First-principles calculations of zero-field splitting parameters, *J. Chem. Phys.*, 2006, **125**, 024103; (c) R. Maurice, R. Bastardis, C. D. Graaf, N. Suaud, T. Mallah and N. Guihéry, Universal

- theoretical approach to extract anisotropic spin hamiltonians, *J. Chem. Theory Comput.*, 2009, **5**, 2977-2984.
34. F. Neese, F. Efficient and accurate approximations to the molecular spin-orbit coupling operator and their use in molecular g-tensor calculations. *J. Chem. Phys.* 2005, **122**, 034107.
- 35.- T. Nakajima, The Douglas–Kroll–Hess Approach. *Chem. Rev.* 2012, **112**, 385-402.
- 36.- J. Jung, M. Atanasov and F. Neese, Ab initio ligand-field theory analysis and covalency trends in actinide and lanthanide free ions and octahedral complexes, *Inorg Chem.*, 2017, **56**, 8802-8816.
- 37.- (a) P. Stock, P., T. Pedzinski, N. Spintig, A. Grohmann, G. Hörner, G. High Intrinsic Barriers against Spin-State Relaxation in Iron(II)-Complex Solutions. *Chem. Eur. J.* 2013, **19**, 839–842.
- (b) I. Trapp, M. W. Löble, J. Meyer, F. Breher, Copper complexes of tripodal κ -6N-donor ligands: A structural, EPR spectroscopic and electrochemical study. *Inorg. Chim. Acta* 2011, **374**, 373–384.
- 38.- J. C. Knight, S. Alvarez, A., J. Amoroso, P. G. Edwards, N. Singha, A novel bipyridine-based hexadentate tripodal framework with a strong preference for trigonal prismatic co-ordination geometries, *Dalton Trans.*, 2010,**39**, 3870-3883.
- 39.-M. Llunell, D. Casanova, J. Cirera, P. Alemany, S. Alvarez, SHAPE, v2.1, Universitat de Barcelona, Barcelona, Spain, 2013.